# Design on a Rational Basis of High-Affinity Peptides Inhibiting the Histone Chaperone ASF1

May Bakail, Albane Gaubert, Jessica Andreani, Gwenaëlle Moal, Guillaume Pinna, Ekaterina Boyarchuk, Marie-Cécile Gaillard, Régis Courbeyrette, Carl Mann, Jean-Yves Thuret, et al.

Article

Cell Chemical Biology

# Design on a Rational Basis of High-Affinity Peptides Inhibiting the Histone Chaperone ASF1

## Graphical Abstract

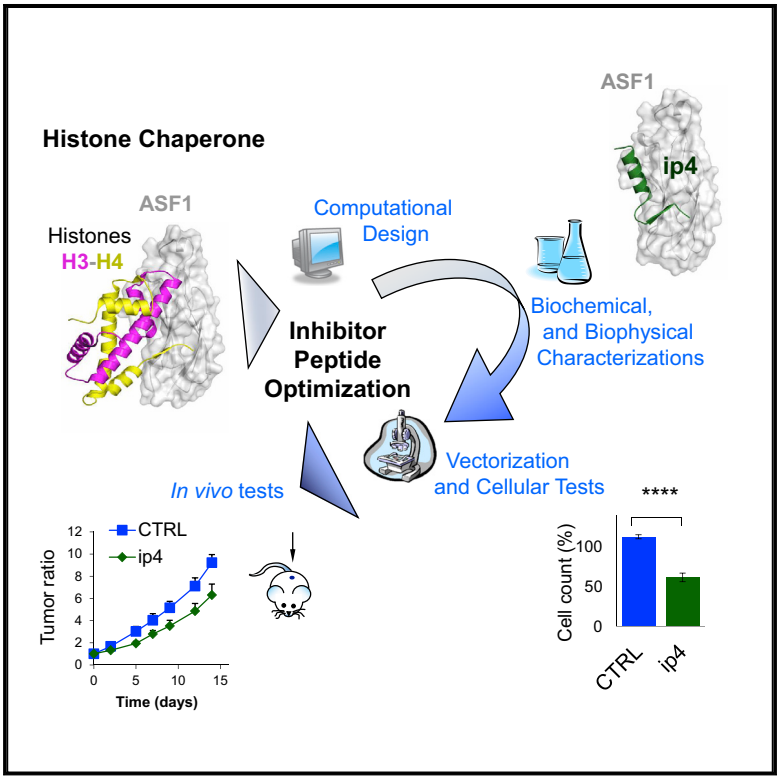


## Highlights

- Development of a computational pipeline for the design of high-affinity peptides
- Epitope tethering and contacts optimization lead to nanomolar ASF1-binding peptides
- The optimal peptide inhibited cell proliferation and perturbed cell cycle
- Injected in mouse allografts, it reduced tumor growth and induced apoptosis

## Authors

May Bakail, Albane Gaubert, Jessica Andreani, ..., Nadia Cherradi, Raphael Guerois, Françoise Ochsenbein

## Correspondence

raphael.guerois@cea.fr (R.G.), francoise.ochsenbein@cea.fr (F.O.)

## In Brief

Bakail et al. developed a strategy for designing peptide inhibitors of protein-protein interactions, based on tethering binding epitopes to increase their affinity and specificity. This strategy was applied to the inhibition of the histone chaperone ASF1, which is essential for the early steps of chromatin assembly and represents a novel target in cancer research.

Bakail et al., 2019, Cell Chemical Biology *26*, 1573–1585
November 21, 2019 
https://doi.org/10.1016/j.chembiol.2019.09.002

CellPress

Cell Chemical Biology
Article

# Design on a Rational Basis of High-Affinity Peptides Inhibiting the Histone Chaperone ASF1

May Bakail,[1,2,8,11] Albane Gaubert,[1,11] Jessica Andreani,[1,2] Gwenaëlle Moal,[1,2] Guillaume Pinna,[1,2] Ekaterina Boyarchuk,[6,7] Marie-Cécile Gaillard,[1,2] Regis Courbeyrette,[1,2] Carl Mann,[1,2] Jean-Yves Thuret,[1,2] Bérengère Guichard,[1] Brice Murciano,[1] Nicolas Richet,[1] Adeline Poitou,[1] Claire Frederic,[1] Marie-Hélène Le Du,[1,2] Morgane Agez,[1] Caroline Roelants,[3,4,5,9] Zachary A. Gurard-Levin,[6,7,10] Geneviève Almouzni,[6,7] Nadia Cherradi,[3,4,5] Raphael Guerois,[1,2,*] and Françoise Ochsenbein[1,2,12,*]

[1]Institute Joliot, Commissariat à l'énergie Atomique (CEA), Direction de la Recherche Fondamentale (DRF), 91191 Gif-sur-Yvette, France
[2]Institute for Integrative Biology of the Cell (I2BC), CEA, CNRS, Univ. Paris-Sud, Université Paris-Saclay, 91198 Gif-sur-Yvette Cedex, France
[3]Institut National de la Santé et de la Recherche Médicale, Unité 1036, 38000 Grenoble, France
[4]Commissariat à l'Energie Atomique, Institut de Recherche Interdisciplinaire de Grenoble, Biologie du Cancer et de l'Infection, 38000 Grenoble, France
[5]Université Grenoble Alpes, Unité Mixte de Recherche-S1036, 38000 Grenoble, France
[6]Institut Curie, Paris Sciences et Lettres (PSL) Research University, CNRS, UMR3664, Equipe Labellisée Ligue Contre le Cancer, 75005 Paris, France
[7]Sorbonne Universités, UPMC Univ Paris 06, CNRS, UMR3664, 75005 Paris, France
[8]Present address: INSERM, U1016, Institut Cochin, 75014 Paris, France
[9]Present address: Inovarion, Paris, France
[10]Present address: SAMDI Tech, Inc., Chicago, IL 60616, USA
[11]These authors contributed equally
[12]Lead Contact
*Correspondence: raphael.guerois@cea.fr (R.G.), francoise.ochsenbein@cea.fr (F.O.)
https://doi.org/10.1016/j.chembiol.2019.09.002

## SUMMARY

**Anti-silencing function 1 (ASF1) is a conserved H3-H4 histone chaperone involved in histone dynamics during replication, transcription, and DNA repair. Overexpressed in proliferating tissues including many tumors, ASF1 has emerged as a promising therapeutic target. Here, we combine structural, computational, and biochemical approaches to design peptides that inhibit the ASF1-histone interaction. Starting from the structure of the human ASF1-histone complex, we developed a rational design strategy combining epitope tethering and optimization of interface contacts to identify a potent peptide inhibitor with a dissociation constant of 3 nM. When introduced into cultured cells, the inhibitors impair cell proliferation, perturb cell-cycle progression, and reduce cell migration and invasion in a manner commensurate with their affinity for ASF1. Finally, we find that direct injection of the most potent ASF1 peptide inhibitor in mouse allografts reduces tumor growth. Our results open new avenues to use ASF1 inhibitors as promising leads for cancer therapy.**

## INTRODUCTION

The importance of epigenetic defects in the initiation and maintenance of cancer stimulated the targeting of numerous pathways involved in chromatin regulation, including histone-modifying enzymes and histone readers (Helin and Dhanak, 2013). An increasing number of studies revealed connections between cancer and histone chaperones (Burgess and Zhang, 2013; Corpet et al., 2011; Montes de Oca et al., 2015; Polo and Almouzni, 2005). One histone chaperone, FACT (Facilitates Chromatin Transcription), dedicated to H2A-H2B assembly, was recently highlighted as being the main target responsible for the antitumor activity of curaxins, recently discovered anti-cancer compounds (Carter et al., 2015; Gasparian et al., 2011). However, H3-H4 histone chaperones have largely been considered challenging targets to inhibit because of the large interaction surface between them and their histone-binding partners. Emerging data support that among the histone chaperones, ASF1 (Anti-Silencing Function 1) represents a very promising anticancer target (Miknis et al., 2015; Seol et al., 2015). In humans, ASF1 exists as two paralogs, termed ASF1A and ASF1B, that share, on average, 70% sequence identity with 100% identity in the histone-binding surface (Natsume et al., 2007), while the unfolded C-terminal tail is much less conserved (Abascal et al., 2013). The two paralogs have some redundant and some specific functions. They both play critical roles in S-phase progression by associating with newly synthesized histones H3-H4 and parental histones H3-H4 at the replication fork (Groth et al., 2005, 2007; Jasencakova et al., 2010). Yet only ASF1B is largely overexpressed in most proliferating cells tested compared with non-proliferating cells (Abascal et al., 2013; Corpet et al., 2011). Importantly, ASF1B depletion impairs the proliferation of various cancer cell lines, and its upregulation is indicative of poor prognosis in breast cancer (Corpet et al., 2011). Conversely, ASF1A expression is maintained in post-mitotic cells and is overexpressed in liver cancers (Wang et al., 2015). Depletion of ASF1A, but not ASF1B, sensitizes liver

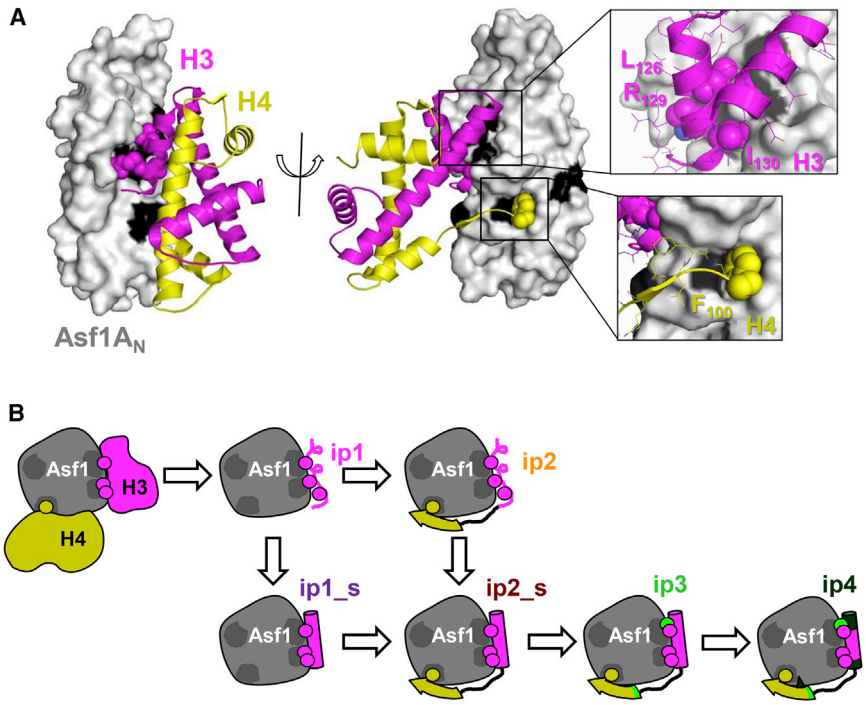


**Figure 1. Schematic Representation of the Design Strategy**

(A) Structure of ASF1A$_N$ (human ASF1A 1–156 conserved domain) in complex with histones H3-H4 (PDB: 2IO5). ASF1 is shown in gray, histone H3 in magenta, and histone H4 in yellow. Apolar patches on the surface of ASF1 are shown in black on ASF1A$_N$, and the side chains of histone anchor residues as spheres (see STAR Methods). Two insets highlight the details of interactions involving helix α3 of histone H3 and the C-terminal strand of histone H4, respectively.

(B) Schematic representation of the design strategy for the ASF1 inhibitory peptides. Starting from the structure of the chaperone bound to its target, the continuous peptide comprising the largest number of anchor residues (represented as circles) was isolated from histone H3 (inhibitory peptide ip1). Apolar patches are shown as dark-gray patches. The helical conformation of the peptide was stabilized through substitutions (ip1_s), and in parallel, a second binding epitope carrying an additional anchor residue inspired from histone H4 was added (ip2). Combination of both modifications led to the inhibitory peptide ip2_s (Figures 2 and S2). This peptide was further optimized through an iterative procedure (ip3, ip4) based on computational design, building upon the high-resolution structure of ASF1 in complex with either ip2_s or ip3 (Figure 2).

See also Table S1 for the complete list of peptides.

cancer cell lines to doxorubicin, a standard chemotherapy drug (Im et al., 2014). ASF1A is also required for reprogramming of human fibroblasts into pluripotent stem cells (Gonzalez-Munoz et al., 2014), and favors cell migration (Wang et al., 2015).

In this study, we aimed to identify inhibitors of the ASF1-histone H3-H4 interaction and explore their impact on cell proliferation and tumor growth. The ASF1-histone interface offers the most promising target given that it is a critical interaction for nearly all ASF1 functions (Agez et al., 2007; Mousson et al., 2005). Recent success inhibiting protein-protein interactions (PPI) illustrates the feasibility and power of this approach (Bakail and Ochsenbein, 2016; Petta et al., 2016). Notably, the ASF1-histone complex represents a particular challenge. Firstly, the binding affinity is in the nanomolar range (Liu et al., 2012). Secondly, the binding interface is rather flat, extended (1,360 Å$^2$), and exhibits distant shallow pockets (Agez et al., 2007; English et al., 2006; Natsume et al., 2007). This suggests that small-molecule inhibitors, while suitable for inhibiting weak affinity complexes (micromolar range) with small interfaces (less than 900 Å$^2$) and deep binding pockets (Filippakopoulos et al., 2010; Fu et al., 2015), may not be sufficiently potent to inhibit the ASF1-histone complex. Alternatively, peptides offer a promising avenue as PPI inhibitors by competing with helical fragments containing most of a protein's binding sites (Milroy et al., 2014; Modell et al., 2016; Rezaei Araghi and Keating, 2016). Therefore, we tackled this issue by optimizing competitive inhibitory peptides that achieved nanomolar affinities through a specific rational design procedure. We then assessed the functional capacity of our ASF1 competitive peptide inhibitors to impair cancer cell proliferation *in vitro* and cancer growth *in vivo* using mouse allograft models.

## RESULTS

### Isolation of Binding Epitopes and Stabilization of the Bound Conformation

By analyzing the crystal structure of the ASF1-histone H3-H4 interface (Natsume et al., 2007), we identified four residues protruding from histones and acting as binding anchors (Rajamani et al., 2004) known to concentrate most of the binding affinity: residues L$_{126}$, R$_{129}$, and I$_{130}$ in histone H3, and F$_{100}$ in H4 (Figures 1A and S3A). The largest distance between these anchor residues is greater than 26 Å, challenging the possibility of obtaining an inhibitory compound able to compete with all four anchors simultaneously. To do so, we designed peptides carrying these anchor residues and optimized their interaction with ASF1 following the step-by-step approach summarized in Figure 1B.

The first inhibitory peptide, ip1, corresponds to the helical fragment of histone H3 117–131, which contains three anchoring residues (L$_{126}$, R$_{129}$, and I$_{130}$ renumbered in the peptide L$_9$, R$_{12}$, and I$_{13}$, respectively) (Figure 2A and Table S1). Ip1 displays a modest affinity for ASF1A (8.7 ± 0.3 μM) as measured by isothermal titration calorimetry (ITC) (Table 1 and Figure S1A). Isolated ip1 is mainly unfolded but folds into the helical conformation upon ASF1 binding, as we previously reported (Agez et al., 2007). To reduce the conformational entropic cost associated with the "folding upon binding" process, we introduced substitutions to stabilize the helical conformation of the peptide in the absence of ASF1, in particular an N-terminal capping-box structure T$_3$-E$_6$ (Aurora and Rose, 1998) and a salt bridge between residue E$_{12}$ and the i+3/i+4 residues R$_{15}$/R$_{16}$ (Figures 2A and S2A; Table S1). The resulting peptide ip1_s exhibits an increase in the helical content from 6% to 30.5% as determined

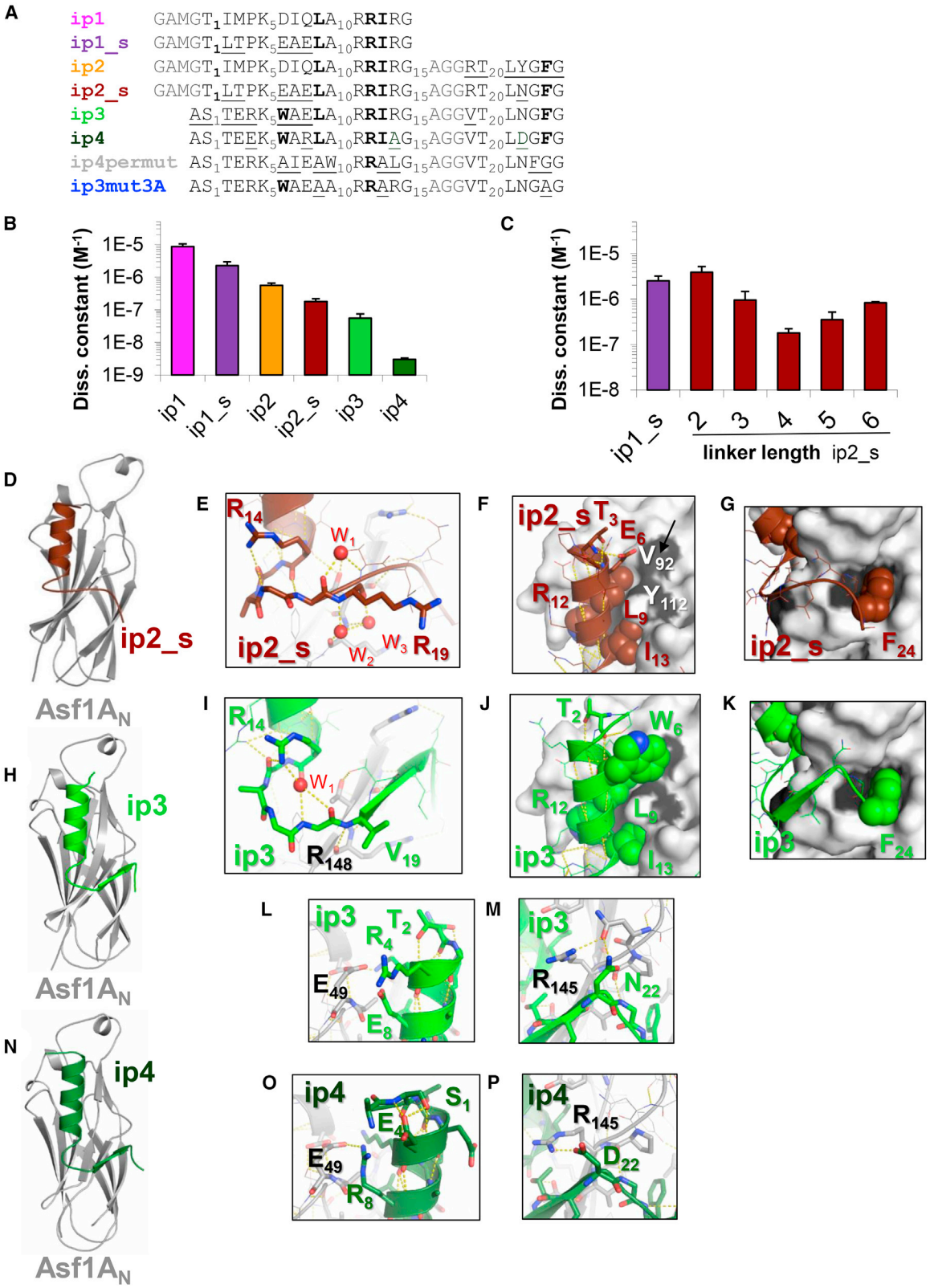


**Figure 2. Optimization toward a Nanomolar Affinity Peptide and *In Vitro* Competition Assay**

(A) Sequences of the main inhibitory peptides designed in the study. Anchor residues are in bold, substitutions are underlined, and linker or tag residues are in gray.

*(legend continued on next page)*

**Table 1. Binding Parameters Measured by Isothermal Microcalorimetry**

| Protein | Peptide | $K_D$ (μM) | $K_D$ ratio$^+$ | $\Delta G$ (kcal M$^{-1}$) | $N^*$ | $\Delta H$ (kcal M$^{-1}$) | $-T\Delta S$ (kcal M$^{-1}$) |
|---|---|---|---|---|---|---|---|
| ASF1AN | ip1 | 8.7 (±0.3) | 1 (±0.1) | −6.4 (±0.2) | 1.1 (±0.1) | −7.4 (±1.1) | 1.0 (±1.1) |
| ASF1AN | ip1_s | 2.2 (±0.7) | 4.3 (±1.6) | −7.2 (±0.2) | 1.1 (±0.1) | −6.4 (±0.4) | −0.7 (±0.6) |
| ASF1AN | ip2 | 0.5 (±0.1) | 15 (±2.9) | −7.9 (±0.2) | 0.98 (±0.01) | −13.0 (±0.4) | 4.8 (±0.6) |
| ASF1AN | ip2_s | 0.18 (±0.04) | 47 (±10) | −8.5 (±0.1) | 1.04 (±0.05) | −11.4 (±1.4) | 2.9 (±1.6) |
| ASF1AN | ip2_s_loop2 | 3.9 (±1.2) | 2.2 (±0.7) | −6.8 (±0.2) | 1.09 (±0.06) | −4.8 (±1.4) | −2.0 (±0.3) |
| ASF1AN | ip2_s_loop3 | 0.95 (±0.5) | 9.2 (±5) | −7.6 (±0.3) | 1.29 (±0.2) | −10.5 (±1.7) | 2.9 (±2.0) |
| ASF1AN | ip2_s_loop5 | 0.35 (±0.16) | 24 (±11) | −8.2 (±0.2) | 1.00 (±0.04) | −11.8 (±1.7) | 3.6 (±1.9) |
| ASF1AN | ip2_s_loop6 | 0.83 (±0.44) | 10.5 (±5) | −7.7 (±0.3) | 1.03 (±0.06) | −7.3 (±0.9) | −0.3 (±1.2) |
| ASF1AN | ip2_s_m1 | 0.23 (±0.015) | 38 (±3) | −8.4 (±0.0.4) | 1.13 (±0.4) | −10.7 (±0.4) | 2.2 (±0.4) |
| ASF1AN | ip2_s_m2 | 0.22 (±0.01) | 39 (±2) | −8.4 (±0.02) | 1.18 (±0.03) | −9.1 (±0.07) | 0.6 (±0.1) |
| ASF1AN | ip2_s_m3 | 0.029 (±0.01) | 304 (±65) | −9.6 (±0.1) | 1.14 (±0.07) | −13.1 (±0.1) | 3.5 (±0.2) |
| ASF1AN | ip2_s_m4 | 0.4 (±0.06) | 21 (±3) | −8.1 (±0.1) | 1.17 (±0.04) | −8.3 (±0.2) | 0.2 (±0.3) |
| ASF1AN | ip3 | 0.055 (±0.02) | 245 (±176) | −9.4 (±0.4) | 1.09 (±0.1) | −14.8 (±1.5) | 5.3 (±1.9) |
| ASF1AN | ip3_m1 | 0.020 (±0.001) | 432 (±16) | −9.8 (±0.04) | 1.05 (±0.05) | −14.9 (±0.7) | 5.1 (±0.7) |
| ASF1AN | ip3_m2 | 0.027 (±0.001) | 326 (±21) | −9.6 (±0.03) | 1.13 (±0.7) | −13.7 (±0.7) | 4.1 (±0.05) |
| ASF1AN | ip3_m3 | 0.010 (±0.002) | 886 (±243) | −10.2 (±0.1) | 1.00 (±0.05) | −15.1 (±1.2) | 4.9 (±1.3) |
| ASF1AN | ip4 | 0.003 (±0.001) | 2,732 (±966) | −10.8 (±0.2) | 1.08 (±0.02) | −13.9 (±0.7) | 3.0 (±0.9) |
| ASF1AN | ip3_mut3A | undetectable | ND | ND | ND | ND | ND |
| ASF1AN | RRP5 | undetectable | ND | ND | ND | ND | ND |
| ASF1BN | ip1 | 5.3(±1.2) | 1 (±0.3) | −6.7 (±0.1) | 0.98 (±0.07) | −8.2 (±0.7) | 1.5 (±0.8) |
| ASF1BN | ip1_s | 3.9 (±0.2) | 1.3 (±0.3) | −6.8 (±0.02) | 1.02 (±0.03) | −8.2 (±0.4) | 1.4 (±0.4) |
| ASF1BN | ip2 | 0.31 (±0.1) | 17.2 (±4.1) | −8.2 (±0.02) | 1.03 (±0.08) | −9.3 (±1.1) | 1.0 (±1.2) |
| ASF1BN | ip2_s | 0.41 (±0.1) | 12.9 (±3.1) | −8.1 (±0.05) | 1.07 (±0.1) | −10.6 (±1.7) | 2.5 (±1.8) |
| ASF1BN | ip3 | 0.093 (±0.007) | 57 (±14) | −8.9 (±0.02) | 1.02 (±0.03) | −14.8 (±1.8) | 5.9 (±1.9) |
| ASF1BN | ip4 | 0.002 (±0.0006) | 2,307 (±829) | −11.0 (±0.1) | 0.92 (±0.1) | −14.4 (±0.9) | 3.5 (±1.0) |
| ASF1BN | ip3_mut3A | undetectable | ND | ND | ND | ND | ND |

Parameters are indicated for the different peptides analyzed in this study (Table S1) with the conserved domain of human ASF1A, ASF1AN (ASF1A 1–156), or human ASF1B, ASF1BN (ASF1B 1–156) as indicated in the first column.

by circular dichroism and nuclear magnetic resonance (Figures S2B and S2C), and a 4-fold higher affinity for ASF1A$_N$ (2.2 ± 0.7 μM) (Figures 2B and S1A; Table 1).

## Epitope Tethering

The affinity of ip1_s for ASF1 remains modest compared with the nanomolar-range affinity of ASF1 with histones H3-H4 (Scorgie et al., 2012), because ASF1 makes many more contacts with the full-length histones. We therefore lengthened the peptide to include the histone H4-binding epitope with residue F$_{100}$. Given the relative orientation of the H3 and H4 fragments with the shortest Cα-Cα distance between the two fragments being 8.6 E (between residues H3-R$_{131}$ and H4-R$_{95}$), we designed an optimal tether to bridge the C terminus of the histone H3 helix to the N terminus of the histone H4 β strand. Statistical analyses (see STAR Methods) predicted that a 4-residue length tether would best match the structural constraints (Figure S3B), and indeed we found it to correspond to the tether length yielding the highest-affinity peptide (Figure 2C). The resulting ip2 peptide exhibited an affinity of 500 ±

(B) Dissociation constants between the conserved domain ASF1A$_N$ and the inhibitory peptides (ip1 to ip4), as measured by isothermal calorimetry (ITC).
(C) Dissociation constants between ASF1A$_N$ and peptides with various linker lengths derived from ip1_s (see Table S1 for the peptide sequences, Table 1 for details of the ITC measurements, and Figure S3B for the prediction of loop length).
(D, H, and N) Overall crystal structures of ASF1A$_N$ (in gray) in complex with the inhibitory peptides ip2_s in brown (D), ip3 in green (H), and ip4 in dark green (N). See Table S2 for data collection and refinement statistics of the three crystal structures presented.
(E and I) Detailed view of the region corresponding to the loop linking the two binding epitopes in the ASF1A$_N$-ip2_s (E) and ASF1A$_N$-ip3 (I) structures.
(F and J) Detailed view of the region corresponding to the binding helical part of the inhibitory peptides in the ASF1A$_N$-ip2_s (F) and the ASF1A$_N$-ip3 (J) structures.
(G and K) Detailed view of the region corresponding to the binding of the C-terminal strand in the ASF1A$_N$-ip2_s (G) and ASF1A$_N$-ip3 (K) structures. View orientations in (F), (J), (G), and (K) are identical to those in detailed regions of the ASF1A$_N$-H3-H4 complex presented in Figure 1A.
(L and O) Detailed view of the region corresponding to the helix capping of the inhibitory peptides ip3 (L) and ip4 (O) in complex with ASF1A$_N$.
(M and P) Detailed view of the region corresponding to the C-terminal extended part of the inhibitory peptides ip3 (M) and ip4 (P) in complex with ASF1A$_N$.
In all magnified panels, ASF1A$_N$ is represented as a gray surface with apolar patches colored in dark gray. Inhibitory peptide ip2_s is colored brown, ip3 green, and ip4 dark green. Anchor residue side chains are highlighted as labeled spheres. Other residues discussed in the text are labeled accordingly. Selected water molecules are shown as red spheres and labeled with a "W." The network of hydrogen bonds is depicted by yellow dashed lines.

100nM, corresponding to a 15-fold gain in affinity with respect to ip1 (Figures 2B and S1B; Table 1).

Next, combining the helix stabilization properties of ip1_s and the tether of ip2 led to peptide ip2_s, which resulted in added stabilization effects and a global affinity gain of nearly 50-fold with respect to the initial ip1 peptide, corresponding to a dissociation constant ($K_D$) of 180 ± 40 nM (Table 1). This gain is almost the product of two independent gains obtained from ip1 to ip1_s (factor 4.3 ± 1.6) and from ip1 to ip2 (factor 15 ± 2.9), which would correspond to a gain of (64 ± 4.5). Thus, the affinity increase was achieved by a coupling between two independent optimizations steps.

## Structure of the Submicromolar ip2_s in Complex with ASF1

We next solved the structure of ASF1A$_N$ in complex with ip2_s by X-ray crystallography at 2.0-Å resolution (Figure 2D and Table S2). The region matching the fragment from histone H3 (117–131) adopts a helical conformation superimposable with the corresponding histone H3 region in the full ASF1-H3-H4 complex (Natsume et al., 2007) (backbone root-mean-square deviation of 1.3 Å between both helices, Figure S2D). As expected, the three anchor residues $L_9$, $R_{12}$, and $I_{13}$ make contacts with ASF1 apolar patches at the same positions as the corresponding histone residues (Figures 1A and 2F). The $F_{24}$ anchor residue added in the second interaction docks into the ASF1A$_N$ pocket similarly to $F_{100}$ in histone H4 (Figures 1A and 2G). Thus, epitope tethering successfully reconstituted anchor positions involved in ASF1 apolar patch binding. However, thorough inspection of the ASF1A$_N$-ip2_s structure revealed two opportunities to further strengthen the interaction between the peptide and ASF1: (1) ASF1A$_N$ $V_{92}$ and $Y_{112}$ residues, which belong to the apolar patch buried by histone H3 α2 and α3 helices remain partially exposed in the ip2_s-ASF1 complex (Figure 2F), and (2) the tether between the N- and C-terminal anchors makes poor contacts with ASF1 due to two water molecules inserted between the ASF1 and ip2_s backbones and forming water bridges that disrupt the canonical β-sheet structure (Figure 2E).

## Interface Optimization on a Rational Basis

To explore these opportunities for optimization via substitutions, we adapted a computational design protocol from those available in the Rosetta software suite (Fleishman et al., 2011). Based on the structure of the ASF1A$_N$-ip2_s complex, we systematically explored the effect of individual substitutions at all positions in ip2_s with the aim of improving its binding affinity for ASF1A$_N$. The heatmap shown in Figure S3C reports the predicted affinity variations for all 20 substitutions. These data led to the design of ip3, which incorporates several substitutions predicted to increase its affinity for ASF1.

We first experimentally tested the impact of the substitution $E_6W$, predicted to bring the largest stabilization effect by further burying $V_{92}$ and $Y_{112}$ in the interface (Figure 2F). Surprisingly, this substitution had minimal impact on binding ($K_D$ of 223 ± 15 nM for ip2_s_m1 compared with 180 ± 40 nN for ip2_s, Tables 1 and S1). The original residue, $E_6$, was initially introduced during the design from ip1 to ip1_s, to act as a capping-box stabilizer residue in position i+3 with respect to the N-cap residue $T_3$ described above (Aurora and Rose, 1998). We hypothesized that the substitution $E_6W$ may have destabilized the capping conformation. We therefore explored the possibility of shifting the N-cap residue $T_3$ by one position toward the N terminus of the peptide. This shift, obtained by substituting the "$L_2T_3PKE_6$" motif by the "$T_2E_3RKE_6$" sequence, had little impact on the affinity (ip2_s_m2, $K_D$ of 220 ± 10 nM, Tables 1 and S1). However, introducing the $E_6W$ substitution in the context of the shifted sequence "$T_2E_3RKW_6$" led to an 8-fold gain in affinity (ip2_s_m3, $K_D$ of 29 ± 10 nM, Tables 1 and S1). We next solved the structure of the ASF1A$_N$-ip3 complex at 2.3-Å resolution (Figure 2H and Table S2) and found that most of the effects anticipated for the substitutions are observed in the experimental structure. Residue $T_2$ acts as an N-cap of the helix, and $W_6$ nicely packs against the ASF1A$_N$ $V_{92}$ side chain and $Y_{112}$ aromatic ring (Figure 2J).

In addition to this $E_6W$ substitution, the ip3 sequence also includes a substitution in the region where two water molecules formed interfacial water bridges in ip2_s. Suggested by the *in silico* screening (Figure S3C), we introduced the $R_{19}V$ substitution to potentially favor an extended conformation. The structure of the ASF1A$_N$-ip3 complex reveals that the β strand $V_{19}$-$N_{22}$ now docks to ASF1A$_N$ by forming direct hydrogen bonds without water-bridge molecules as in ip2_s (Figures 2I and 2K). Even if the $R_{19}V$ substitution brings no stabilization for ASF1A$_N$ binding (ip2_s_m4, $K_D$ of 400 ± 60 nM, Tables 1 and S1), it stabilizes the strand pairing with ASF1 and removes the GR motif that is known to increase sensitivity to trypsin–like proteases. Altogether, the resulting ip3 peptide (Figure 2A) binds ASF1A$_N$ with higher affinity ($K_D$ of 55 ± 20 nM), corresponding to an approximate 5-fold gain of affinity with respect to ip2_s (Figure 2B and S1C; Table 1).

In-depth analysis of the ASF1A$_N$-ip3 structure identified additional opportunities for optimization. Based on these data, we tested three additional sets of substitutions: (1) ip3_$E_8$R_$R_4$E, which alleviates repulsive interactions between $E_8$ in ip3 and the acidic loop of ASF1 ($E_{49}$-$D_{54}$); (2) ip3_$R_{14}$A, which removes an "RG" motif prone to degradation by serum proteases; and (3) ip3_$N_{22}$D, which creates an additional salt bridge with ASF1 $R_{145}$. Combined together, the three sets of substitutions led to a peptide called ip4 (Figure 2A), which exhibits a potent affinity for ASF1 ($K_D$ = 3 ± 1 nM) (Figures 2B and S1C) similar to that measured between ASF1 and the full histone H3-H4 complex (Scorgie et al., 2012). We then solved the structure of the ASF1A$_N$-ip4 complex at 1.98-Å resolution (Figure 2N and Table S2). As anticipated based on structural modeling, residues $R_8$ and $D_{22}$ in ip4 are found in salt-bridge interactions with ASF1A$_N$ residues $E_{49}$ and $R_{145}$, respectively (Figures 2O and 2P), accounting for the increased affinity obtained for the ip4 peptide. Of note, we measured similar binding affinities for all peptides with ASF1A$_N$ and ASF1B$_N$ (Figure S2E and Table 1), consistent with the fact that ASF1A and ASF1B share 100% sequence identity in their histone interaction surface.

## Inhibitory Peptides Selectively Associate with ASF1 and Disrupt the ASF1-Histone Interaction *In Vitro* and in Cell Extracts

We first designed a control peptide with reduced binding affinity for ASF1 while keeping the sequence as close as possible to ip3 and ip4. This peptide, called ip3mut3A, includes three substitutions of anchoring residues $L_9$, $I_{13}$, and $F_{24}$ to alanine and in our

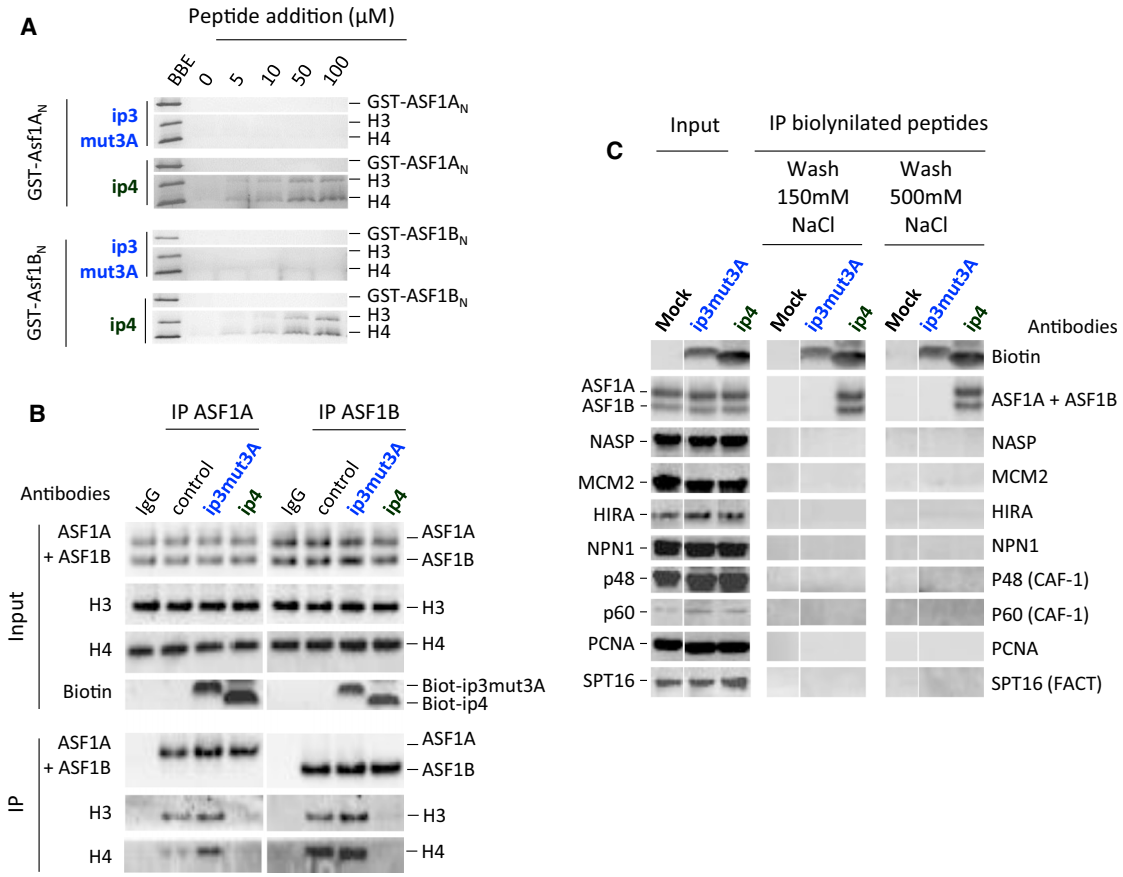


**Figure 3. ip4 Selectively Associates with ASF1 and Dissociates the ASF1-Histone Interaction *In Vitro* and in Cell Extracts**

(A) GST pull-down competition experiments. The conserved domains of ASF1A or ASF1B, fused to GST, were bound to beads and complexed to full-length H3-H4 histones. Dissociation of histones H3 and H4 upon addition of inhibitory peptide was monitored by SDS-PAGE colored with silver staining. For comparison, beads before elution with the inhibitory peptide (BBE) were also analyzed. The absence of dissociation of GST-ASF1A and ASF1B from beads is also shown.

(B and C) Immunoprecipitation of ASF1A or ASF1B from cellular extracts after incubation, with biotinylated ip3mut3A, ip4, or without peptide (control) (B). Histones H3 and H4 co-immunoprecipitated with ASF1 were revealed by western blotting with the antibodies indicated in the left legend. Immunoprecipitation with immunoglobulin G was used as negative control. (C) Pull-down of biotinylated peptides ip4 and ip3mut3A from cell extracts. The washing steps were performed with two different salt concentrations as indicated. Proteins eluted with an excess of biotin were revealed with different antibodies as indicated in the right legend. Further analysis of bound proteins is presented in Figure S4 and Table S3.

assays shows no detectable binding for ASF1A$_N$ or ASF1B$_N$ (Figures 2Aand S1D; Table 1). We assessed the inhibitory activity of the active and control peptides *in vitro* by measuring their capacity to dissociate histones previously bound to glutathione *S*-transferase (GST)-ASF1A$_N$ or GST-ASF1B$_N$ beads. As shown in Figure 3A, ip4 dissociates histones in a concentration-dependent manner while the control peptide ip3mut3A does not. We estimate that the elution corresponded around 30% of the bound histones at the highest peptide concentration tested. The capacity of ip4 to disrupt the Asf1-histone complex was further assessed in a cellular context (Figure 3B). We used cellular extracts previously incubated (or not) with ip4 and measured the presence of histones H3 and H4 co-immunoprecipitated with anti-ASF1A or anti-ASF1B antibodies after electrophoresis followed by western blotting. The presence of ip4, compared with the control peptide ip3mut3A, clearly led to a decrease in the amount of histones H3-H4 associated with endogenous ASF1A and ASF1B.

Given that the peptides recapitulate a histone-like surface, their capacity to interact with other known histone chaperones or histone-binding proteins was analyzed by pull-down experiments from cellular extracts with biotinylated peptides. Proteins bound to biotin-ip4 or biotin-ip3mut3A were revealed by western blotting using different antibodies including the histone chaperones ASF1, NASP (Nuclear Autoantigenic Sperm Protein), MCM2 (Mini Chromosome Maintenance 2), HIRA (Histone Regulation A), NPN1 (Nucleophosmin 1), the subunits p48 and p60 of CAF-1 (Chromatin Assembly Factor 1), FACT, or the DNA polymerase processing factor PCNA (Proliferating Cell Nuclear Antigen) (Figure 3C). Remarkably, only ASF1A and ASF1B were associated with Biotin-ip4, and none of the tested chaperones interacted with biotin-ip3mut3A.

To further validate the selectivity of ip4 for ASF1 in cell extracts, we quantitatively analyzed all proteins bound to biotin-ip4 or biotin-ip3mut3A using mass spectrometry in three independent replicates (Figure S4). Both ASF1A and ASF1B were detected in the top-ten list among the proteins specifically purified with ip4 and not ip3mut3A, with ASF1B in the top two

(Table S3). Thus, ASF1A and ASF1B are, as anticipated, among the main binders of ip4 in cellular extracts.

### GFP-Tagged Inhibitory Peptides Target ASF1-Histone Interaction in U2OS Human Osteosarcoma Cells

As a first approach to evaluate the biological activity of the inhibitory peptides, plasmids encoding GFP-tagged peptides ip3, ip4, or the negative control ip3mut3A peptide were transfected into human osteosarcoma U2OS cell lines (Figure 4A) (STAR Methods). The localization of the fusion proteins was visualized by florescence microscopy (Figures S5A–S5C). For comparison, we used a GFP-H3 expression plasmid (Galvani et al., 2008) for overexpression of full histone H3 fused to GFP. While GFP-H3 is found mainly in the nucleus, GFP-coupled inhibitory peptides are localized in the whole cell and can thus reach Asf1, which is mainly located in the nucleus but also associated with cytosolic histones (Campos et al., 2010, 2015). Co-immunoprecipitation assays were performed 48 h after transfection to confirm the interaction between inhibitory peptides and Asf1 proteins in the cells (Figure 4B). Although the peptides were significantly degraded in cells, with an important proportion of visible degradation products of GFP immunoprecipitated proteins (Figure 4B), both ASF1A and ASF1B co-immunoprecipitated efficiently with GFP-ip3 or GFP-ip4 in a similar manner to the positive control histone H3, while none of the two ASF1 proteins was detected with the negative control GFP-ip3mut3A (Figure 4B).

To measure the biological activity of the ASF1 peptide inhibitors, we measured cell proliferation/survival upon transient expression of GFP-ip3, GFP-ip4, or GFP-ip3mut3A 24 h after transfection by cell count using high-content fluorescence microscopy (see STAR Methods). We observed a significant reduction in the number of cells with GFP-ip3 and GFP-ip4 plasmids (Figure 4C) compared with GFP-transfected cells (74% ± 7% and 61% ± 5%, respectively), while the peptide GFP-ip3mut3A did not reduce the total number of cells (112% ± 3% compared with GFP-transfected cells). Similar results were obtained using standard proliferation viability MTT (methyl thiazolyl tetrazolium) tests as described above (Figure S5D). Interestingly, we measured a similar decrease in the number of cells after transfection with a combination of small interfering RNAs (siRNAs) against ASF1A + ASF1B (Figures S6A–S6C), but this effect was not significant with each siRNA alone (Figure S6C).

To further assess the specificity of the inhibitory activity on ASF1, we assessed the cell-cycle profile using the nuclear fluorescence signal of Hoechst-stained cells (see STAR Methods). Twenty-four hours after transient expression of GFP, GFP-ip3, GFP-ip4, or GFP-ip3mut3A, we observed a significant increase in the population of cells in S phase with a decrease in the population of cells in $G_1$ after expression of GFP-ip3 or GFP-ip4 compared with the control cells (Figure 4D). The same trend is observed after transfection with a combination of siRNAs against ASF1A + ASF1B (Figure S6D). The distribution analysis of cells in the different cell-cycle phases was further refined using a double labeling detected by flow cytometry (see STAR Methods). After expression of GFP-ip3 and GFP-ip4 compared with control cells, we observed a significant increase in the proportion of cells in gates labeled "slow S" and "S-arrested" corresponding to replicating cells according to their intermediate DNA content, but incorporating less bromodeoxyuridine (BrdU) or no BrdU, respectively (Figure 4E). Such accumulation of cells in the "slow S" panel was also observed, although to a greater extent, after treatment with a combination of siRNA against ASF1A and ASF1B (Figure S6E). We conclude that expression of the Asf1 inhibitory peptides is associated with loss of function of ASF1, similar to that observed after treatment with siRNA targeting ASF1. However, the peptides proved less efficient compared with siRNA, possibly because they are subject to proteolytic degradation in cells as observed in the GFP pull-down assays (Figure 4E).

### ASF1 Inhibitors Vectorized with a Cell-Penetrating Tag Reduce U2OS Cell Viability and Perturb the Cell Cycle

We next tested the biological activity of the ASF1 peptide inhibitors transduced as external compounds in U2OS cell lines. For this, we lengthened the peptides at their N terminus with a cell-penetrating peptide sequence (CPP) (Figure 5A and Table S1). We chose the repeat tag sequence "RRPRRPRRPRRPRRP" as it has been shown to enter cells with high efficiency (Daniels and Schepartz, 2007). Twenty-four hours after simple addition of the ASF1-inhibitor peptides in the culture media, we measured a significant decrease in the number of cells associated with a dose-response-dependent effect ranging from 1 μM to 10 μM for the cells treated with CPP-ip3 and CPP-ip4 compared with the non-treated cells (67% ± 4% and 67% ± 4%, for CPP-ip3 and CPP-ip4, respectively, at 10 μM) (Figure 5B). Notably, treatment with the control peptide CPP-ip3mut3A showed no significant effect at these concentrations when compared with untreated cells.

We next explored the impact of CPP-vectorized peptides on U2OS cell-cycle progression using the fluorescence signal of Hoechst-stained cells. A slight but reproducible decrease in the proportion of cells in $G_1$ phase was measured with CPP-ip3 and CPP-ip4 but not CPP-ip3mut3A (Figure 5C). Interestingly, this trend is similar to the one previously observed after plasmid nucleofection coding for the GFP-peptide constructs (Figure 4D), suggesting that this effect is a specific consequence of the peptide activity in cells.

### Cell-Penetrating Inhibitory Peptides Impair Migration and Invasion of Aggressive Breast Cancer Cells *In Vitro* and Inhibit Tumor Growth *In Vivo*

Based on the above findings, we extended our investigation to determine whether the inhibitory peptides could exert antitumor activity *in vitro* and *in vivo*. Before evaluating the therapeutic potential of CPP-ip3mut3A, CPP-ip3, and CPP-ip4 peptides, we tested their capacity to reduce 4T1 mouse mammary tumor cell proliferation after direct addition to the culture medium (Figure 6A). As shown in Figure 6B, CPP-ip3 and CPP-ip4 exhibited significantly reduced proliferation in this cell line at concentrations of 20–30 μM. In contrast, the control peptide CPP-ip3mut3A showed no detectable effect on cell proliferation up to 30 μM.

We investigated the ability of CPP-ip3 and CPP-ip4 to inhibit migration and invasion of cancer cells, two important processes in cancer progression and metastasis. We used a peptide concentration of 10 μM, below the concentration that impairs cell proliferation. The control CPP-ip3mut3A peptide has a mild and non-significant effect on fetal bovine serum-induced cell migration as compared with vehicle (Figures 6C and S7A) while treatment with CPP-ip3 or CPP-ip4 decreases cell migration by 75% and 85%,

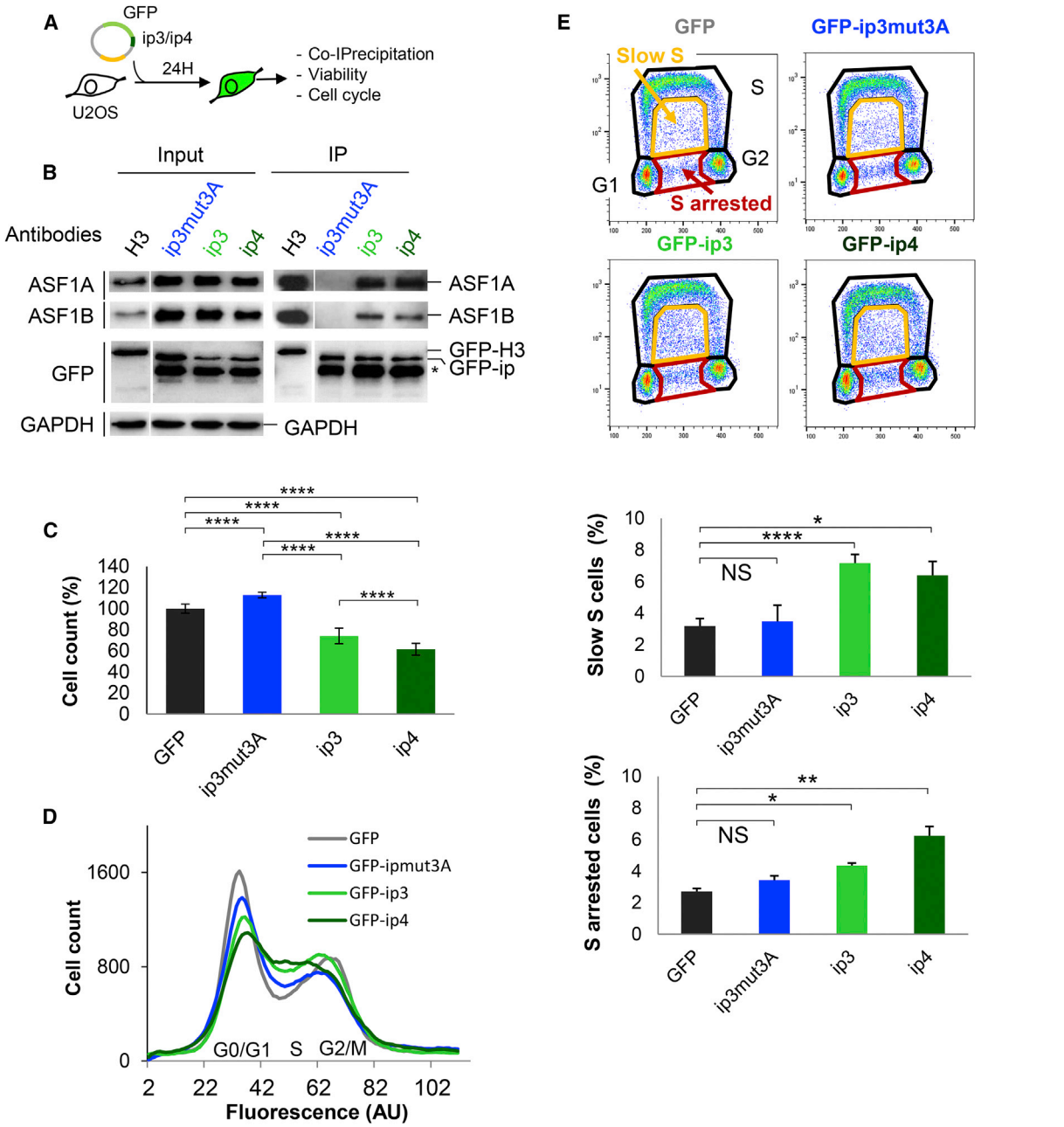


**Figure 4. Co-immunoprecipitation, Cell Viability, and Cell-Cycle Analysis of U2OS Cells Nucleofected with a Plasmid Expressing the Inhibitory Peptides Fused to GFP**

(A) U2OS cells were nucleofected with a plasmid coding a GFP fluorescent fusion with inhibitory peptides (see STAR Methods and Figure S5).

(B) Western blot analysis of GFP-peptides co-immunoprecipitated with ASF1 proteins from U2OS total extracts revealed by the antibodies indicated in the left legend. A plasmid expressing H3-GFP was used as a positive control of interaction with ASF1A and ASF1B. GAPDH and GFP were immunodetected as controls of sample loading and peptide expression, respectively. The star indicates the GFP-degraded peptide.

(C) Adherent cell count 24 h after plasmid nucleofection. Data are displayed as a percentage with respect to the number of control cells transfected with the control vector expressing only the GFP. Values correspond to means ± SEM of three experiments with six replicates in each experiment (18 replicates in total).

(D) Cell-cycle profiles from fluorescence cell imaging. Curves represent the distribution of nuclear DNA content in the population as intervals of Hoechst fluorescence intensity.

(E) Flow-cytometry analysis of cell-cycle distribution in asynchronous cells 24 h after plasmid nucleofection. U2OS cells were labeled with propidium iodide (x axis) and bromodeoxyuridine (BrdU) (y axis). Gates used for quantifications are indicated by colored boxes. Quantification of the "slow S" cells and "S-arrested" cells are shown in the lower panel. Values are expressed as means ± SEM of two independent experiments, three replicates in total.

In (C) and (E), significance was determined by a t test: ****$p < 0.0001$, **$p \leq 0.005$, *$p \leq 0.05$; NS, not significant.

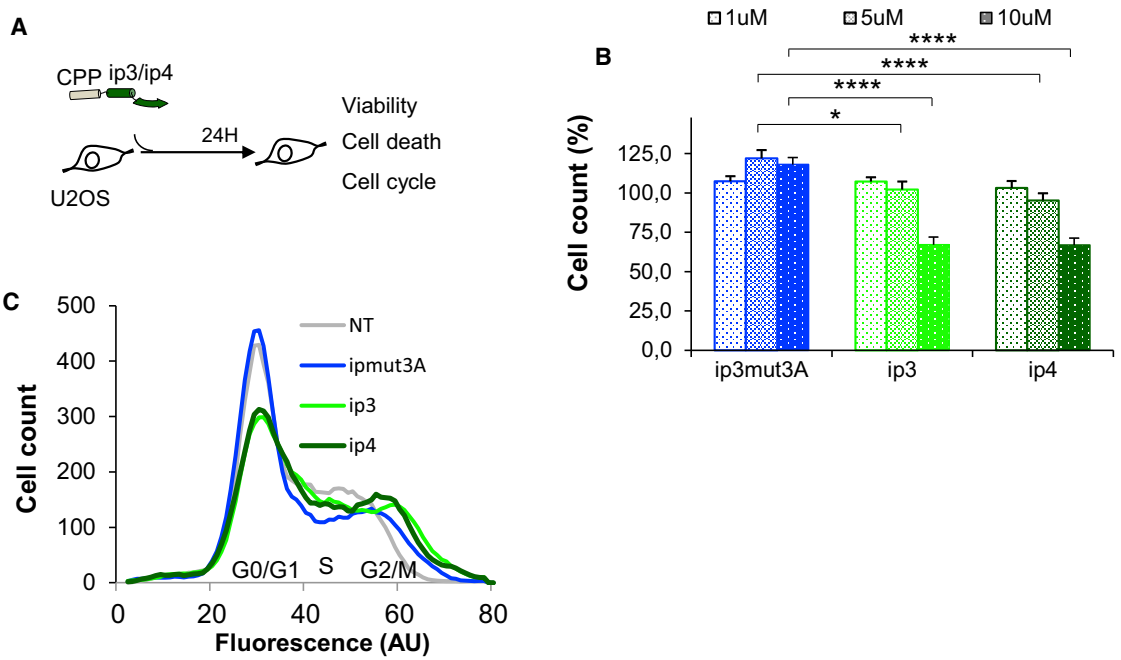


**Figure 5. Vectorized Inhibitory Peptides Reduce U2OS Cell Viability and Perturb the Cell Cycle**

(A) Cell-penetrating (CPP) vectorized peptides (see Table S1 for the sequence of CPP-vectorized peptides) were directly added into the cell-culture medium. Viability, cell count, and cell-cycle distribution were analyzed 24 h after incubation of cells at 37°C (STAR Methods).

(B) Cell count after treatment with the corresponding CPP-vectorized peptides. Data are expressed as percentage of untreated control cells. Values correspond to means ± SEM of five independent experiments, 14 replicates in total. Significance determined by Student's t test: ****$p \leq 0.0001$, *$p \leq 0.05$.

(C) Cell-cycle profiles from fluorescence cell imaging. Curves represent the distribution of nuclear DNA content in the population as intervals of Hoechst fluorescence, measured 24 h after addition of 10 μM of the corresponding peptides in the cell-culture medium. NT, non-treated cells.

respectively. CPP-ip3 and CPP-ip4 impair 4T1 cell invasion relative to the control peptide (Figures 6D and S7A). These results suggest that both CPP-ip3 and CPP-ip4 peptides markedly affect signaling pathways involved in cancer cell motility.

To investigate the ability of CPP-ip3 and CPP-ip4 peptides to decrease tumor growth *in vivo*, we used the syngeneic 4T1 mammary tumor model in immunocompetent BALB/c mice (Figure 6E). As shown in Figure 6F, at day 14 post implantation, CPP-ip3 and CPP-ip4 significantly inhibit 4T1 tumor growth by 32% compared with vehicle or CPP-ip3mut3A peptide (n = 5 for each group). We also performed immunohistochemical analyses on resected tumors to assess tumoral hypoxia and vascular endothelial growth factor (VEGF) expression, two major positive regulators of tumor angiogenesis (Figures 6G and S7B). We observed a striking decrease in intratumoral hypoxia (glucose transporter 1 staining) and VEGF expression upon treatment with CPP-ip3 and CPP-ip4 peptides, while CPP-ip3mut3A had little effect compared with vehicle (Figure 6G). Next, we detected a diffuse cytoplasmic active caspase-3 staining in CPP-ip3-treated cells and an even stronger signal in CPP-ip4-treated cells (Figure 6G), indicating that CPP-ip3 and CPP-ip4 peptides promote tumor cell death through apoptosis. Notably, the strong nuclear staining for PCNA observed in vehicle and CPP-ipmut3A-treated tumors is markedly decreased upon CPP-ip3 and CPP-ip4 treatment. Collectively, these results suggest that in addition to their inhibitory effect on cell proliferation, CPP-ip3 and CPP-ip4 peptides are able to efficiently impair major cancer hallmarks.

## DISCUSSION

In this work, we designed ASF1 peptide inhibitors through an iterative process to optimize their affinity for ASF1. The nanomolar affinity of ip4 for ASF1 resembles the affinity of the ASF1-(H3-H4) complex, a favorable condition for competing with this interaction in cells. The high affinity of the peptides described here is unmatched by small molecules reported to inhibit the ASF1-histone complex (Miknis et al., 2015; Seol et al., 2015). Through our success in the design of high-affinity compounds, we demonstrate how computational predictions coupled to structural analysis can serve the practical goal of finding inhibitory peptides for protein interfaces of interest. One key step toward increasing the binding affinity in the design protocol came from the tethering of two binding epitopes. Such a strategy is reminiscent of the fragment-tethering strategy proposed for small molecules to increase the affinity for their target (Erlanson et al., 2004; Modell et al., 2016; Scott et al., 2013). α helices have been extensively studied as starting motifs to design peptide inhibitors (Guarracino et al., 2011; Modell et al., 2016). As one step forward, the use of two coupled epitopes including a β strand is a major novelty of the present design. The tether was designed by inserting a loop whose length was simply derived from statistical analysis of existing structures. As a generalization of this tethering strategy, we found that about 10% of all structurally characterized complexes (Faure et al., 2012) exhibit such a spatial configuration (see STAR Methods). This suggests that the motif comprising

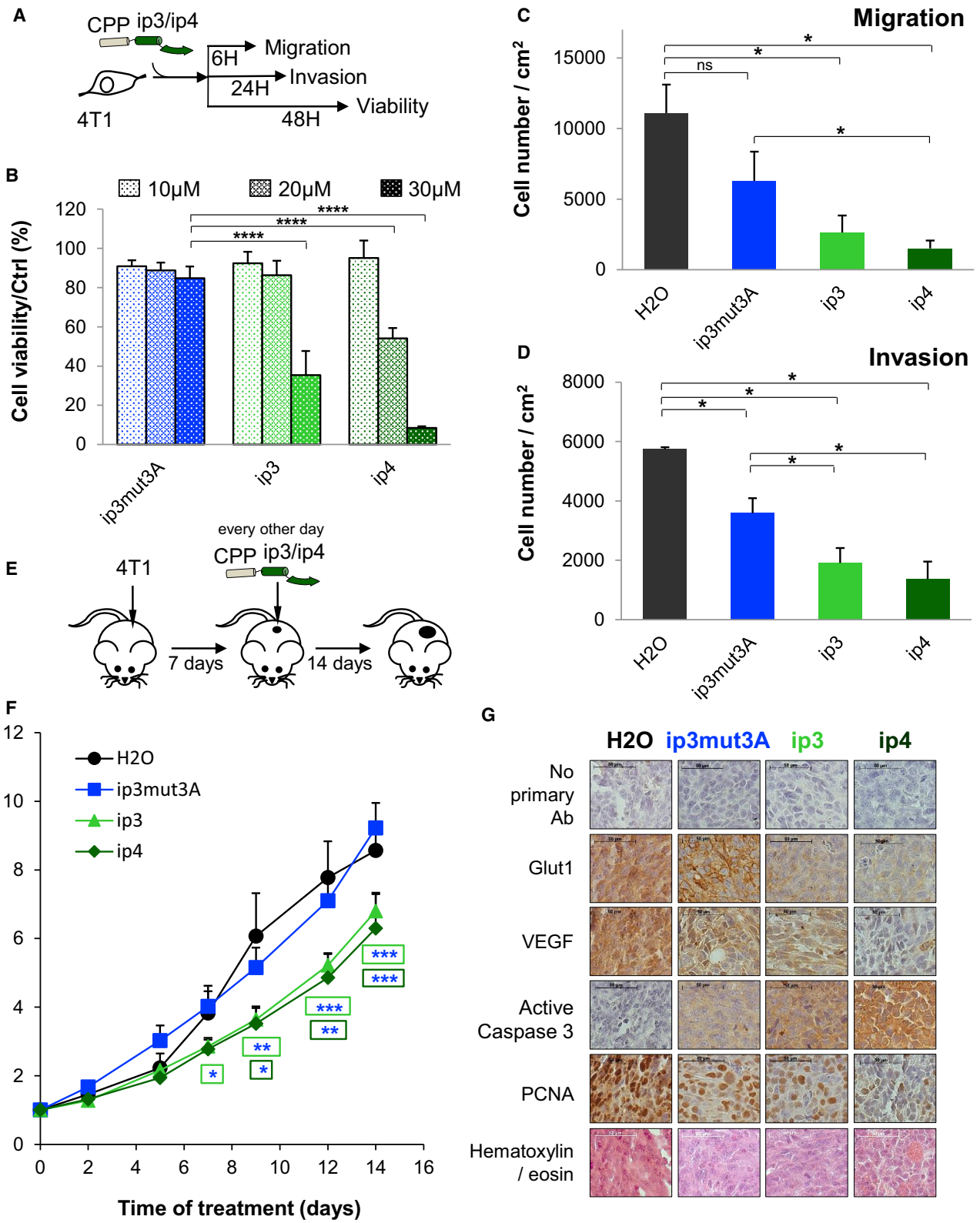


**Figure 6. ASF1 Inhibitory Peptides Impair Migration and Invasion of Aggressive Breast Cancer Cells *In Vitro* and Inhibit Tumor Growth *In Vivo***

(A) Cell-penetrating vectorized peptide was internalized by adding the peptide directly into the culture medium of mouse 4T1 cells. Migration, invasion, and cell viability were measured as indicated.

*(legend continued on next page)*

a helix tethered with a small strand could be used as a potent scaffold in a significant number of interfaces with a strategy similar to the one developed to inhibit ASF1.

The designed peptides are able to compete with histones H3-H4 in binding to ASF1, *in vitro* both with purified proteins (Figure 3A) and in cell extracts (Figure 3B). Given that the peptides have structural similarities with some histone parts, to check their specificity for ASF1 we could exclude association with other well-known histone-binding proteins (Figure 3C). Furthermore, quantitative mass spectrometry analyses (Table S3 and Figure S4) confirmed that ASF1A and ASF1B belong to the top ten binders of ip4 and that the interactions of the peptides with ASF1s are sequence specific, as none of these two proteins were associated with the control peptide ip3mut3A. These observations do not exclude that some off-target effects could be in part responsible for the observed phenotypes. Nevertheless, the designed inhibitory peptides have phenotypic effects similar to those produced by siRNA knockdown of ASF1A + ASF1B mRNAs, namely, a cytotoxic/cytostatic effect in human and mouse cancer cells, and a block in cell-cycle progression of U2OS cells with a depletion of cells in $G_1$, and an accumulation of cells in S phase (Figure S6) (Corpet et al., 2011; Groth et al., 2007). Notably, we observe the significant cellular response regardless of the method used to introduce or express the inhibitory peptides in cells, as a plasmid coding for the peptides (Figures 4 and S5) or as peptides vectorized by a cell-penetrating tag (Figure 5). These results suggest that the reduced proliferation/viability and cell-cycle perturbations could be attributed to the inhibition of both proteins ASF1A and ASF1B in cells. Our study also explores the potential antitumor effect of inhibiting ASF1 (Figure 6). We observe a significant decrease of breast cancer cell migration and invasion after treatment with the inhibitory peptides, suggesting that ASF1 is involved in pathways regulating cancer cell motility. Tumor growth is significantly reduced after direct injection of peptides in syngeneic grafted tumors in mice. Immunohistochemical analyses revealed that common tumor hallmarks are strongly decreased after treatment with CPP-ip3 or CPP-ip4. Although we cannot rule out that some other effects could contribute to the reduction in tumor growth, this pilot study provides the first indication that inhibitory peptides targeting the histone chaperones ASF1A/ASF1B can be designed effectively to produce antitumoral effects, and provides new tools to further study ASF1 function.

## SIGNIFICANCE

**The importance of epigenetic defects in cancer initiation and maintenance has stimulated intensive research aiming to target different pathways involved in histone metabolism, including histone-modifying enzymes or histone readers. Histone chaperones, however, have proved difficult to target despite their well-established links to cancer initiation and progression. So far, only one active molecule in cancer treatment has been identified retrospectively to target the FACT histone chaperone. Here, we focused on the histone chaperone ASF1 (Anti-Silencing Function 1), involved in histone H3-H4 dynamics during DNA replication, transcription, and DNA repair, and displaying specialized functions during cell-cycle progression. Notably, ASF1 is overexpressed in many cancer cells, and its depletion severely compromised cell proliferation, suggesting that inhibiting the interaction between ASF1 and histones could have unique anticancer effects. However, the interface of the ASF1-H3H4 complex, lacking significant cavity and showing distant hotspot residues (26 Å), is a difficult target. In this work, we overcame this difficulty by combining computational design with structural and thermodynamic characterizations of synthetic peptide inhibitors bound to ASF1. We demonstrated the potency of these compounds as competitors for histone binding by ASF1 *in vitro* and in cell extracts. Furthermore, we used several strategies to deliver these peptides in cancer cell lines, and thereby demonstrated their abilities to perturb cell-cycle progression and reduce cell proliferation in a manner similar to depletion of ASF1 by siRNA. Finally, using mouse allograft models, we confirmed that our highest-affinity peptide for ASF1 has a potent inhibitory effect on tumor growth *in vivo*.**

## STAR★METHODS

Detailed methods are provided in the online version of this paper and include the following:

- KEY RESOURCES TABLE
- LEAD CONTACT AND MATERIALS AVAILABILITY
- EXPERIMENTAL MODEL AND SUBJECT DETAILS
  - Human Cell Lines
  - In Vivo Animal Studies

(B) Assessment of cell viability using PrestoBlue assay. Data are expressed as percentage of cell viability measured in non-treated control cells and are presented as mean ± SEM of three independent experiments performed in triplicates (****$p < 0.0001$, significantly different from control cells, Mann-Whitney test).
(C and D) Transwell migration (C) and invasion (D) assays of 4T1 cells treated with $H_2O$ or with 10 μM of ip3mut3A, ip3, or ip4 peptides. Values are expressed as mean ± SEM of three independent experiments (*$p < 0.05$, Mann-Whitney U test). See also Figure S7A.
(E and F) Effect of ASF1 inhibitory peptides on tumor growth. (E) 4T1 cells were implanted subcutaneously into BALB/c immunocompetent mice. When the subcutaneous tumors reached 50–100 $mm^3$ in size (day 7 post implantation), mice were randomized into four groups and vehicle ($H_2O$), ip3mut3A, ip3, or ip4 peptides were injected every other day into the tumors (100 μg/injection). Tumor size was monitored by caliper measurement of tumor length and width every other day as described in STAR Methods. The experiment was terminated after 14 days of treatment. Results (F) are expressed as the ratio of the tumor volume to the value at the starting time point (t = 0). Statistically significant differences were determined between the ip3mut3A-treated group (blue) and the ip3- or the ip4-treated groups (light and dark green, respectively). n = 5 for each group. *$p < 0.05$, **$p < 0.01$, ***$p < 0.001$ (Mann-Whitney test).
(G) Histochemical hematoxylin and eosin staining and immunohistochemical detection of tumor hypoxic areas (glucose transporter 1 [Glut1]), intratumoral vascular endothelial growth factor (VEGF), apoptosis (active caspase-3), and proliferation (proliferating cell nuclear antigen [PCNA]) in the untreated group ($H_2O$) and each treated group (ip3mut3A, ip3, and ip4) after 14 days of treatment. The antibody-negative control (no primary Ab) was performed to exclude non-specific immunohistochemical staining. Scale bar, 50 μm. All images were captured at 40× magnification.
See also Figure S7B.

## SUPPLEMENTAL INFORMATION

Supplemental Information can be found online at https://doi.org/10.1016/j.chembiol.2019.09.002.

## ACKNOWLEDGMENTS

We thank the Synchrotron Soleil (Proxima 1 and Proxima 2 beam lines) and in particular Pierre Legrand for his help in crystallography, the European Synchrotron Radiation Facility (ESRF), the French Infrastructure for Integrated Structural Biology (FRISBI), Arnaud Martel for the computing facility, Vasily Ogryzko and François Leteurtre for their advice on cell biology, and M. Bourges from I2BC for its help at the flow-cytometry platform. We thank Florent Dingli and Damarys Loew from Institut Curie mass spectrometry and proteomics facility for carrying out the MS experimental work, and D.L. for supervising MS and data analysis. The project was supported by the ARC, France 2009 CR109/8006 2016 PGA1 20160203953, ANR, France BREAKABOUND 2007, BIPBIP 2011, CHAPINHIB 2012, and CHIPSET 2015, M.B. was supported by Canceropole, Paris, France, and a grant for young researchers from La Ligue contre le Cancer, France.

## AUTHOR CONTRIBUTIONS

Conceptualization, R.G. and F.O.; Methodology, J.A., G.P., C.M., N.C., R.G., and F.O.; Software, J.A. and R.G.; Validation, A.P., C.F., Z.A.G.-L., R.G., and F.O.; Formal Analysis, C.R. and F.O.; Investigation, M.B., A.G., G.M., G.P., E.B., M.-C.G., R.C., B.G., B.M., N.R., M.A., C.R., N.C., R.G., and F.O.; Resources, J.-Y.T. and G.A.; Writing – Original Draft, M.B., A.G., J.A., N.C., R.G., and F.O.; Writing – Review & Editing, J.A., G.P., E.B., M.-C.G., R.G., and F.O.; Supervision, C.M., G.P., J.-Y.T., M.-H.L.D., G.A., N.C., R.G., and F.O.; Project Administration, F.O.; Funding Acquisition, Z.A.G.-L., G.A., N.C., R.G., and F.O.

## DECLARATION OF INTERESTS

A patent based on results from this paper has been deposited by the CEA and Université Paris VI and published with the number 20150025016 with A.G., R.C., R.G., and F.O. as inventors. The other authors declare no competing interests.

Received: June 13, 2018
Revised: June 12, 2019
Accepted: September 3, 2019
Published: September 19, 2019

## REFERENCES

Abascal, F., Corpet, A., Gurard-Levin, Z.A., Juan, D., Ochsenbein, F., Rico, D., Valencia, A., and Almouzni, G. (2013). Subfunctionalization via adaptive evolution influenced by genomic context: the case of histone chaperones ASF1a and ASF1b. Mol. Biol. Evol. *30*, 1853–1866.

Agez, M., Chen, J., Guerois, R., van Heijenoort, C., Thuret, J.Y., Mann, C., and Ochsenbein, F. (2007). Structure of the histone chaperone ASF1 bound to the histone H3 C-terminal helix and functional insights. Structure *15*, 191–199.

Andreani, J., Faure, G., and Guerois, R. (2012). Versatility and invariance in the evolution of homologous heteromeric interfaces. PLoS Comput. Biol. *8*, e1002677.

Aurora, R., and Rose, G.D. (1998). Helix capping. Protein Sci. *7*, 21–38.

Bakail, M., and Ochsenbein, F. (2016). Targeting protein–protein interactions, a wide open field for drug design. C. R. Chim. *19*, 19–27.

Bricogne, G., Blanc, E., Brandl, M., Flensburg, C., Keller, P., Paciorek, W., Roversi, P., Sharff, A., Smart, O.S., Vonrhein, C., et al. (2017). BUSTER Version 2.10 (Global Phasing Ltd).

Burgess, R.J., and Zhang, Z. (2013). Histone chaperones in nucleosome assembly and human disease. Nat. Struct. Mol. Biol. *20*, 14–22.

Campos, E.I., Fillingham, J., Li, G., Zheng, H., Voigt, P., Kuo, W.H., Seepany, H., Gao, Z., Day, L.A., Greenblatt, J.F., et al. (2010). The program for processing newly synthesized histones H3.1 and H4. Nat. Struct. Mol. Biol. *17*, 1343–1351.

Campos, E.I., Smits, A.H., Kang, Y.H., Landry, S., Escobar, T.M., Nayak, S., Ueberheide, B.M., Durocher, D., Vermeulen, M., Hurwitz, J., et al. (2015). Analysis of the histone H3.1 interactome: a suitable chaperone for the right event. Mol. Cell *60*, 697–709.

Carter, D.R., Murray, J., Cheung, B.B., Gamble, L., Koach, J., Tsang, J., Sutton, S., Kalla, H., Syed, S., Gifford, A.J., et al. (2015). Therapeutic targeting of the MYC signal by inhibition of histone chaperone FACT in neuroblastoma. Sci. Transl. Med. *7*, 312ra176.

Cook, A.J., Gurard-Levin, Z.A., Vassias, I., and Almouzni, G. (2011). A specific function for the histone chaperone NASP to fine-tune a reservoir of soluble H3-H4 in the histone supply chain. Mol. Cell *44*, 918–927.

Corpet, A., De Koning, L., Toedling, J., Savignoni, A., Berger, F., Lemaitre, C., O'Sullivan, R.J., Karlseder, J., Barillot, E., Asselain, B., et al. (2011). Asf1b, the necessary Asf1 isoform for proliferation, is predictive of outcome in breast cancer. EMBO J. *30*, 480–493.

Daniels, D.S., and Schepartz, A. (2007). Intrinsically cell-permeable miniature proteins based on a minimal cationic PPII motif. J. Am. Chem. Soc. *129*, 14578–14579.

Deutsch, E.W., Csordas, A., Sun, Z., Jarnuczak, A., Perez-Riverol, Y., Ternent, T., Campbell, D.S., Bernal-Llinares, M., Okuda, S., Kawano, S., et al. (2017). The ProteomeXchange consortium in 2017: supporting the cultural change in proteomics public data deposition. Nucleic Acids Res. *45*, D1100–D1106.

Emsley, P., and Cowtan, K. (2004). Coot: model-building tools for molecular graphics. Acta Crystallogr. D Biol. Crystallogr. *60*, 2126–2132.

English, C.M., Adkins, M.W., Carson, J.J., Churchill, M.E., and Tyler, J.K. (2006). Structural basis for the histone chaperone activity of Asf1. Cell *127*, 495–508.

Erlanson, D.A., McDowell, R.S., and O'Brien, T. (2004). Fragment-based drug discovery. J. Med. Chem. *47*, 3463–3482.

Faure, G., Andreani, J., and Guerois, R. (2012). InterEvol database: exploring the structure and evolution of protein complex interfaces. Nucleic Acids Res. *40*, D847–D856.

Filippakopoulos, P., Qi, J., Picaud, S., Shen, Y., Smith, W.B., Fedorov, O., Morse, E.M., Keates, T., Hickman, T.T., Felletar, I., et al. (2010). Selective inhibition of BET bromodomains. Nature *468*, 1067–1073.

Fleishman, S.J., Leaver-Fay, A., Corn, J.E., Strauch, E.M., Khare, S.D., Koga, N., Ashworth, J., Murphy, P., Richter, F., Lemmon, G., et al. (2011). RosettaScripts: a scripting language interface to the Rosetta macromolecular modeling suite. PLoS One *6*, e20161.

Fu, L.L., Tian, M., Li, X., Li, J.J., Huang, J., Ouyang, L., Zhang, Y., and Liu, B. (2015). Inhibition of BET bromodomains as a therapeutic strategy for cancer drug discovery. Oncotarget *6*, 5501–5516.

Galvani, A., Courbeyrette, R., Agez, M., Ochsenbein, F., Mann, C., and Thuret, J.Y. (2008). In vivo study of the nucleosome assembly functions of ASF1 histone chaperones in human cells. Mol. Cell. Biol. *28*, 3672–3685.

Gasparian, A.V., Burkhart, C.A., Purmal, A.A., Brodsky, L., Pal, M., Saranadasa, M., Bosykh, D.A., Commane, M., Guryanova, O.A., Pal, S., et al. (2011). Curaxins: anticancer compounds that simultaneously suppress NF-kappaB and activate p53 by targeting FACT. Sci. Transl. Med. *3*, 95ra74.

Gonzalez-Munoz, E., Arboleda-Estudillo, Y., Otu, H.H., and Cibelli, J.B. (2014). Cell reprogramming. Histone chaperone ASF1A is required for maintenance of pluripotency and cellular reprogramming. Science *345*, 822–825.

Groth, A., Corpet, A., Cook, A.J., Roche, D., Bartek, J., Lukas, J., and Almouzni, G. (2007). Regulation of replication fork progression through histone supply and demand. Science *318*, 1928–1931.

Groth, A., Ray-Gallet, D., Quivy, J.P., Lukas, J., Bartek, J., and Almouzni, G. (2005). Human Asf1 regulates the flow of S phase histones during replicational stress. Mol. Cell *17*, 301–311.

Guarracino, D.A., Bullock, B.N., and Arora, P.S. (2011). Mini review: protein-protein interactions in transcription: a fertile ground for helix mimetics. Biopolymers *95*, 1–7.

Helin, K., and Dhanak, D. (2013). Chromatin proteins and modifications as drug targets. Nature *502*, 480–488.

Hubbard, S.J., and Thornton, J.M. (1993). NACCESS. Computer Program Department of Biochemistry and Molecular Biology (University College London).

Im, J.S., Keaton, M., Lee, K.Y., Kumar, P., Park, J., and Dutta, A. (2014). ATR checkpoint kinase and CRL1betaTRCP collaborate to degrade ASF1a and thus repress genes overlapping with clusters of stalled replication forks. Genes Dev. *28*, 875–887.

Jacak, R., Leaver-Fay, A., and Kuhlman, B. (2012). Computational protein design with explicit consideration of surface hydrophobic patches. Proteins *80*, 825–838.

Jasencakova, Z., Scharf, A.N., Ask, K., Corpet, A., Imhof, A., Almouzni, G., and Groth, A. (2010). Replication stress interferes with histone recycling and predeposition marking of new histones. Mol. Cell *37*, 736–743.

Kabsch, W., and Sander, C. (1983). Dictionary of protein secondary structure: pattern recognition of hydrogen-bonded and geometrical features. Biopolymers *22*, 2577–2637.

Kabsch, W. (2010). Integration, scaling, space-group assignment and post-refinement. Acta Crystallogr. D Biol. Crystallogr. *66*, 133–144.

Lacroix, E., Viguera, A.R., and Serrano, L. (1998). Elucidating the folding problem of alpha-helices: local motifs, long-range electrostatics, ionic-strength dependence and prediction of NMR parameters. J. Mol. Biol. *284*, 173–191.

Leaver-Fay, A., Tyka, M., Lewis, S.M., Lange, O.F., Thompson, J., Jacak, R., Kaufman, K., Renfrew, P.D., Smith, C.A., Sheffler, W., et al. (2011). ROSETTA3: an object-oriented software suite for the simulation and design of macromolecules. Methods Enzymol. *487*, 545–574.

Lijnzaad, P., Berendsen, H.J., and Argos, P. (1996). A method for detecting hydrophobic patches on protein surfaces. Proteins *26*, 192–203.

Liu, W.H., Roemer, S.C., Port, A.M., and Churchill, M.E. (2012). CAF-1-induced oligomerization of histones H3/H4 and mutually exclusive interactions with Asf1 guide H3/H4 transitions among histone chaperones and DNA. Nucleic Acids Res. *40*, 11229–11239.

Merutka, G., Dyson, H.J., and Wright, P.E. (1995). 'Random coil' 1H chemical shifts obtained as a function of temperature and trifluoroethanol concentration for the peptide series GGXGG. J. Biomol. NMR *5*, 14–24.

Miknis, G.F., Stevens, S.J., Smith, L.E., Ostrov, D.A., and Churchill, M.E. (2015). Development of novel Asf1-H3/H4 inhibitors. Bioorg. Med. Chem. Lett. *25*, 963–968.

Milroy, L.G., Grossmann, T.N., Hennig, S., Brunsveld, L., and Ottmann, C. (2014). Modulators of protein-protein interactions. Chem. Rev. *114*, 4695–4748.

Modell, A.E., Blosser, S.L., and Arora, P.S. (2016). Systematic targeting of protein-protein interactions. Trends Pharmacol. Sci. *37*, 702–713.

Montes de Oca, R., Gurard-Levin, Z.A., Berger, F., Rehman, H., Martel, E., Corpet, A., de Koning, L., Vassias, I., Wilson, L.O., Meseure, D., et al. (2015). The histone chaperone HJURP is a new independent prognostic marker for luminal A breast carcinoma. Mol. Oncol. *9*, 657–674.

Mosmann, T. (1983). Rapid colorimetric assay for cellular growth and survival: application to proliferation and cytotoxicity assays. J. Immunol. Methods *65*, 55–63.

Mousson, F., Couprie, J., Thuret, J.Y., Neumann, J.M., Mann, C., and Ochsenbein, F. (2004). $^{1}H$, $^{13}C$ and $^{15}N$ resonance assignments of the conserved core of hAsf1 A. J. Biomol. NMR *29*, 413–414.

Mousson, F., Lautrette, A., Thuret, J.Y., Agez, M., Courbeyrette, R., Amigues, B., Becker, E., Neumann, J.M., Guerois, R., Mann, C., et al. (2005). Structural basis for the interaction of Asf1 with histone H3 and its functional implications. Proc. Natl. Acad. Sci. U S A *102*, 5975–5980.

Nakatani, Y., and Ogryzko, V. (2003). Immunoaffinity purification of mammalian protein complexes. Methods Enzymol. *370*, 430–444.

Natsume, R., Eitoku, M., Akai, Y., Sano, N., Horikoshi, M., and Senda, T. (2007). Structure and function of the histone chaperone CIA/ASF1 complexed with histones H3 and H4. Nature *446*, 338–341.

Petta, I., Lievens, S., Libert, C., Tavernier, J., and De Bosscher, K. (2016). Modulation of protein-protein interactions for the development of novel therapeutics. Mol. Ther. *24*, 707–718.

Polo, S.E., and Almouzni, G. (2005). Histone metabolic pathways and chromatin assembly factors as proliferation markers. Cancer Lett. *220*, 1–9.

Poullet, P., Carpentier, S., and Barillot, E. (2007). myProMS, a web server for management and validation of mass spectrometry-based proteomic data. Proteomics *7*, 2553–2556.

Rajamani, D., Thiel, S., Vajda, S., and Camacho, C.J. (2004). Anchor residues in protein-protein interactions. Proc. Natl. Acad. Sci. U S A. *101*, 11287–11292.

Rezaei Araghi, R., and Keating, A.E. (2016). Designing helical peptide inhibitors of protein-protein interactions. Curr. Opin. Struct. Biol. *39*, 27–38.

Richet, N., Liu, D., Legrand, P., Velours, C., Corpet, A., Gaubert, A., Bakail, M., Moal-Raisin, G., Guerois, R., Compper, C., et al. (2015). Structural insight into how the human helicase subunit MCM2 may act as a histone chaperone together with ASF1 at the replication fork. Nucleic Acids Res. *43*, 1905–1917.

Schwarzinger, S., Kroon, G.J., Foss, T.R., Chung, J., Wright, P.E., and Dyson, H.J. (2001). Sequence-dependent correction of random coil NMR chemical shifts. J. Am. Chem. Soc. *123*, 2970–2978.

Scorgie, J.K., Donham, D.C., 3rd, and Churchill, M.E. (2012). Analysis of histone chaperone antisilencing function 1 interactions. Methods Enzymol. *512*, 223–241.

Scott, D.E., Ehebauer, M.T., Pukala, T., Marsh, M., Blundell, T.L., Venkitaraman, A.R., Abell, C., and Hyvonen, M. (2013). Using a fragment-based approach to target protein-protein interactions. Chembiochem *14*, 332–342.

Seol, J.H., Song, T.Y., Oh, S.E., Jo, C., Choi, A., Kim, B., Park, J., Hong, S., Song, I., Jung, K.Y., et al. (2015). Identification of small molecules that inhibit the histone chaperone Asf1 and its chromatin function. BMB Rep. *48*, 685–690.

Smart, O.S., Womack, T.O., Flensburg, C., Keller, P., Paciorek, W., Sharff, A., Vonrhein, C., and Bricogne, G. (2012). Exploiting structure similarity in refinement: automated NCS and target-structure restraints in BUSTER. Acta Crystallogr. D Biol. Crystallogr. *68*, 368–380.

Vagin, A., and Teplyakov, A. (2010). Molecular replacement with MOLREP. Acta Crystallogr. D Biol. Crystallogr. *66*, 22–25.

Vagin, A.A., Steiner, R.A., Lebedev, A.A., Potterton, L., McNicholas, S., Long, F., and Murshudov, G.N. (2004). REFMAC5 dictionary: organization of prior chemical knowledge and guidelines for its use. Acta Crystallogr. D Biol. Crystallogr. *60*, 2184–2195.

Valot, B., Langella, O., Nano, E., and Zivy, M. (2011). MassChroQ: a versatile tool for mass spectrometry quantification. Proteomics *11*, 3572–3577.

Wang, C., Chang, J.F., Yan, H., Wang, D.L., Liu, Y., Jing, Y., Zhang, M., Men, Y.L., Lu, D., Yang, X.M., et al. (2015). A conserved RAD6-MDM2 ubiquitin ligase machinery targets histone chaperone ASF1A in tumorigenesis. Oncotarget *6*, 29599–29613.

Wang, G., and Dunbrack, R.L., Jr. (2005). PISCES: recent improvements to a PDB sequence culling server. Nucleic Acids Res. *33*, W94–W98.

Yang, G., Chu, W., Zhang, H., Sun, X., Cai, T., Dang, L., Wang, Q., Yu, H., Zhong, Y., Chen, Z., et al. (2013). Isolation and identification of mannose-binding proteins and estimation of their abundance in sera from hepatocellular carcinoma patients. Proteomics *13*, 878–892.

## STAR★METHODS

### KEY RESOURCES TABLE

| REAGENT or RESOURCE | SOURCE | IDENTIFIER |
|---|---|---|
| Antibodies | | |
| ASF1a and ASF1b | (Corpet et al., 2011); Cell Signaling | N/A; Cat# 2902; RRID: AB_2059664; Cat# 2990; RRID: AB_2289918 |
| sNASP | (Cook et al., 2011) | N/A |
| HIRA | Abnova corporation | Cat# MAB8967; RRID: AB_10715607 |
| CAF-1 p60 | NOVUS | Cat# NB500-212; RRID: AB_10001768 |
| CAF-1 p48 | Abcam | Cat# ab1765; RRID: AB_2253589 |
| Biotin | Abcam | Cat# ab53494; RRID: AB_867860 |
| MCM2 | BD Biosciences | Cat# 610700; RRID: AB_2141952 |
| PCNA | Agilent; Abcam | Cat# M0879; RRID: AB_2160651; Cat#ab29; RRID: AB_303394 |
| Nucleophosmin1 NPN1 | Abcam | Cat# ab37659; RRID: AB_2283064 |
| FACT Spt16 | Santa Cruz Biotechnology | Cat# sc-28734; RRID: AB_661341 |
| Histone H3 | Abcam | Cat# ab1791; RRID: AB_302613 |
| Histone H4 | Abcam | Cat# ab18255; RRID: AB_470265 |
| GFP | Abcam | Cat# ab290; RRID: AB_303395 |
| GAPDH | Cell Signaling | Cat# 2118; RRID: AB_561053 |
| BrdU | BD Biosciences | Cat# 347580; RRID: AB_400326 |
| human VEGF-A | Santa Cruz | Cat# Sc-152; RRID: AB_2212984 |
| anti-GLUT1 | Abcam | Cat#ab15309; RRID: AB_301844 |
| cleaved Caspase 3 | Cell Signaling | Cat# 9664; RRID; AB_2070042 |
| Bacterial and Virus Strains | | |
| E. Coli BL21 (DE3) STAR | Invitrogen | Cat#44-0049 |
| Chemicals, Peptides, and Recombinant Proteins | | |
| Custom synthesis service, sequences are given in Table S1 | GeneCust | N/A |
| protease inhibitors cocktails | Roche | Cat#11873580001 |
| phosphatase inhibitors cocktails | Roche | Cat#4906845001 |
| protein A/G resin | ThermoFisher | Cat#53132 |
| Lipofectamine RNAiMAX | Life Technologies | Cat#13778075 |
| protease inhibitors cocktails | Roche | Cat#11873580001 |
| μMACS Anti-GFP MicroBeads | Miltenyi Biotec | Cat#130-091-288 |
| methyl thiazolyl tetrazolium MTT | Sigma Aldrich | M5655 |
| Hoechst 33342 | Sigma | Cat#B2261-25mg |
| Propidium Ionide (PI) | Sigma Aldrich | P4864 |
| Alexa-Fluor 647 Azide | Thermofisher | A10277 |
| Critical Commercial Assays | | |
| Amaxa Cell Line Nucleofector Kit V | Lonza | Cat#VVCA-1003 |
| double labelling with Click-iT 5-ethynyl-2'-deoxyuridine (Click-iT EdU) | Thermofisher | Ca#C10632 |
| PrestoBlue® assay | Thermofischer | A13261 |
| Boyden chamber plates for migration assay | BD Biosciences | #353097 |
| 24-well Matrigel Invasion chamber plates | BD BioSciences | #354480 |

(*Continued on next page*)

*Continued*

| REAGENT or RESOURCE | SOURCE | IDENTIFIER |
|---|---|---|
| Deposited Data | | |
| Mass spectrometry proteomics data for pulldowns with biotinylated peptides ip3mut3A and ip4 | This Study | PXD013279 |
| Coordinates and Map coefficients of ASF1-ip2_s | This Study | 6F0F |
| Coordinates and Map coefficients of ASF1-ip3 | This Study | 6F0G |
| Coordinates and Map coefficients of ASF1-ip4 | This Study | 6F0H |
| Experimental Models: Cell Lines | | |
| HeLa S3 cells | (Nakatani and Ogryzko, 2003) | N/A |
| U2OS (osteosarcoma) cells | ATCC® | HTB-96™ |
| 4T1 murine breast cancer cells | ATCC® | CRL-2539™ |
| Experimental Models: Organisms/Strains | | |
| Mouse Balb/c mice | Janvier Labs | SC-BJ-10S-F |
| Oligonucleotides | | |
| siRNAs against ASF1A | ThermoFisher | ID: s226043 |
| siRNAs against ASF1B | ThermoFisher | ID: s31345 |
| scrambled siRNA | ThermoFisher | Cat#4390843, Silencer Select #1 sequence, |
| Recombinant DNA | | |
| pETM30 plasmid $(His)_6$–GST –Tev site–Asf1 | (Mousson et al., 2004) | N/A |
| pET28 plasmid (His)6-dAsf1-H3-H4 | (Richet et al., 2015) | N/A |
| pDEST53-ip3mut3A | This Study | N/A |
| pDEST53-ip3 | This Study | N/A |
| pDEST53-ip4 | This Study | N/A |
| Software and Algorithms | | |
| NACCESS | (Hubbard and Thornton, 1993) | http://wolf.bms.umist.ac.uk/naccess/ |
| DSSP | (Kabsch and Sander, 1983) | https://swift.cmbi.umcn.nl/gv/dssp/; RRID: SCR_002725 |
| AGADIR | (Lacroix et al., 1998) | http://agadir.crg.es/; RRID: SCR_008402 |
| Rosetta | (Leaver-Fay et al., 2011); (Fleishman et al., 2011) | https://www.rosettacommons.org/software; RRID: SCR_015701 |
| Topspin | Bruker | RRID: SCR_014227 |
| Sparky | (T.D. Goddard and D.G. Kneller, UCSF). | https://nmrfam.wisc.edu/nmrfam-sparky-distribution/; RRID: SCR_014228 |
| MOLREP | (Vagin and Teplyakov, 2010) | Ccp4i suite |
| Coot | Coot | https://www2.mrc-lmb.cam.ac.uk/Personal/pemsley/coot/; RRID: SCR_014222 |
| BUSTER | (Bricogne et al., 2017; Smart et al., 2012) | http://www.globalphasing.com/buster/; RRID: SCR_015653 |
| REFMAC | (Vagin and Teplyakov, 2010; Vagin et al., 2004) | Ccp4i suite; RRID: SCR_014225 |
| PYMOL | Schrödinger | https://pymol.org/2/; RRID: SCR_000305 |
| myProMS | (Poullet et al., 2007) | http://bioinfo-out.curie.fr/myproms/proms.html |
| Prism 7 | GraphPad | https://www.graphpad.com/ |
| Other | | |
| InterEvol database | (Faure et al., 2012) | http://biodev.cea.fr/interevol/interevol.aspx; RRID: SCR_006054 |

## LEAD CONTACT AND MATERIALS AVAILABILITY

Further information and requests for resources and reagents should be directed to and will be fulfilled by the Lead Contact, Françoise Ochsenbein (francoise.ochsenbein@cea.fr).

## EXPERIMENTAL MODEL AND SUBJECT DETAILS

### Human Cell Lines

Human cancer cell lines U2OS (osteosarcoma [ATCC® HTB-96™]) or HeLa S3 (Nakatani and Ogryzko, 2003) were routinely cultured in DMEM (Dulbecco's Modified Eagle Medium; Sigma-Aldrich) containing 10% v/v FBS (Fetal bovine serum; Sigma-Aldrich) and 100U/mL of penicillin, 100μg/mL streptomycin (Gibco) at 37°C in a humidified incubator with 5% $CO_2$. Cells were analyzed within the first seven passages. 4T1 murine breast cancer cells [ATCC® CRL-2539™] were cultured in RPMI 1640 GlutaMAX medium (Invitrogen) containing 10% v/v FBS, 100U/mL of penicillin, 100μg/mL of streptomycin and 30μg/mL gentamicin (Invitrogen) at 37°C in a humidified incubator with 5% $CO_2$.

### In Vivo Animal Studies

Balb/c mice (10 weeks old, 20-25g) were obtained from Janvier Labs (France). Five female mice were used for each group.

## METHOD DETAILS

### Design Methods

#### *Identification of Binding Anchors and Apolar Patches*

Anchors were defined as in (Andreani et al., 2012; Rajamani et al., 2004) as up to three residues from the core and support regions of the interface, which bury the most solvent-accessible surface area (rASA) upon binding and in any case, more than 80Å2 rASA values were assessed for each residue using NACCESS (Hubbard and Thornton, 1993). Apolar patches for each side of the interface were defined as in (Andreani et al., 2012; Jacak et al., 2012; Lijnzaad et al., 1996). They correspond to contiguous regions (based on the α-shape connections between surface interface C and S atoms) containing at least four apolar atoms from at least two different residues.

#### *Protein Database Analysis for Determining the Length of the Linker between the Two Epitopes*

The distribution of loop lengths in protein structures was calculated as a function of the Cα-Cα distance between secondary structure elements in the 7092 chains from the culled pdb database (Wang and Dunbrack, 2005) (percentage identity cut off is 25%, the resolution cut off is 2.5Å, and the R-factor cut off is 0.3). Delimitations of the secondary structures were analysed using DSSP (Kabsch and Sander, 1983). The number of residues in the loop was studied as a function of the Cα-Cα distance between the residues at the extremities of two secondary structures connected by a loop. For every Cα-Cα distance, the frequencies of each size of the loop is reported in Figure S3B.

#### *Methods for Predicting Substitutions*

Initial sequence modifications were introduced according to known helical stabilization elements such as capping motifs (Aurora and Rose, 1998) and other factors studied in the development of the AGADIR program (Lacroix et al., 1998). The automatic approach to guide the choice of a favorable substitution at the corresponding peptide position was based on virtual single substitution scanning. For each complex structure (ASF1A$_N$-ip2_s and ASF1A$_N$-ip3), the first step of the computational protocol involved a minimization of the template structure in the Rosetta force-field starting from the X-ray coordinates (Leaver-Fay et al., 2011). Special options were used to constrain the relaxation in order to minimally affect the coordinates. One representative structure was chosen out of 1,000 generated, on the basis of its Rosetta energy and the size of the cluster associated with it. The position scanning protocol was inspired from and designed using RosettaScripts (Fleishman et al., 2011) (see details and xml file for RosettaScripts below). The protocol contains one mutagenesis step (using the PackRotamersMover mover with a soft repulsive potential and limiting repacking to a 6 Å sphere around the mutated residues) followed by a GenericMonteCarlo mover performing 10 iterations over a design protocol involving a RepackMinimize step with soft repulsive potential, a RepackMinimize step with standard Rosetta potential, a backrub step with standard parameters and a final RepackMinimize scoring step with standard potential. Each substitution was specified by providing a resfile which specifies to use native amino acids (NATAA) except for mutated positions. Options for the repacking also include the use of extra chi1 and chi2 sub-rotamers and the use of native rotamers from the input structure. Each set of substitutions and the corresponding neutral substitution were performed 80 times. The energy differences between mutant and wild-type residue were calculated as Boltzmann-weighted energy differences between each of the 80 mutated models and a reference chosen as the amino acid present in the sequence of the reference structure (ASF1A$_N$-ip2_s or ASF1A$_N$-ip3). The results of these calculations are presented in Figures S3C and S3D for ASF1A$_N$-ip2_s and ASF1A$_N$-ip3, respectively.

### *Script Used for the Scanning of a Specific Position*

(in the example position 232 is scanned for leucine amino-acid, as defined in the Resfile):

Command line:

"$path_to_rosetta_exec/rosetta_scripts.default.linuxgccrelease -s Template.pdb -out:prefix output/score.out -parser:script_vars varresfile=Resfile.res -resfile Resfile.res @Optionfile"

Content of the files used in command line:

**Resfile.res:**

```
NATAA
EX 1 EX 2
USE_INPUT_SC
start
232 B PIKAA L
```

**Optionfile:**

```
-database rosetta_database
-use_input_sc
-ex1
-ex2
-ignore_unrecognized_res
-out::nstruct 80
-jd2:ntrials 1
-parser:protocol Protocole.xml
```

**Protocole.xml:**

```
<dock_design>
<SCOREFXNS>
<scoreXmod weights="talaris2013m">[1]
</scoreXmod>
<softrepmod weights="talaris2013m_softrep">[2]
</softrepmod>
</SCOREFXNS>
<TASKOPERATIONS>
    <InitializeFromCommandline name=init />
    <ReadResfile name=resfin filename="%%varresfile%%" />
<DesignAround name=interface_around resnums=221B,222B,223B,224B,225B,226B,227B,228B,229B,230B,231B,232B,
233B,234B,235B,236B,237B,238B,239B,240B,241Bdesign_shell=6.0 repack_shell=6.0 />
    <DesignAround name=res_around resnums=232B design_shell=6.0 repack_shell=6.0 />
</TASKOPERATIONS>
<FILTERS>
    <Ddg name=ddG scorefxn=scoreXmod threshold=-1 repeats=2 />
    <Sasa name=sasa threshold=800 />
    <CompoundStatement name=ddg_sasa>
        <AND filter_name=ddG />
        <AND filter_name=sasa />
    </CompoundStatement>
</FILTERS>
<MOVERS>
<PackRotamersMover name=mutate scorefxn=softrepmodtask_operations=init,resfin,interface_around/>
    <RepackMinimize name=des1 scorefxn_repack=softrepmod scorefxn_minimize=softrepmodminimize_bb_ch1=0 minimize_
    bb_ch2=1 minimize_rb=0 interface_cutoff_distance=6.0design_partner2=1 design_partner1=0 task_operations=init,resfin,
    res_around />
    <RepackMinimize name=des2 scorefxn_repack=scoreXmod scorefxn_minimize=scoreXmodminimize_bb_ch1=0 minimize_
    bb_ch2=1 minimize_rb=0 interface_cutoff_distance=6.0task_operations=init,resfin,res_around />
    <BackrubDD name=backrub partner1=0 partner2=1 interface_distance_cutoff=8.0moves=1000 sc_move_probability=0.25
    scorefxn=scoreXmod small_move_probability=0.15bbg_move_probability=0.25 task_operations=init,resfin,res_around />
    <ParsedProtocol name=design>
        <Add mover_name=des1 />
        <Add mover_name=des2 />
```

```
        <Add mover_name=backrub />
        <Add mover_name=des2 filter_name=ddg_sasa />
    </ParsedProtocol>
    <GenericMonteCarlo name=iterate scorefxn_name=scoreXmod mover_name=designtrials=10 />
</MOVERS>
<PROTOCOLS>
    <Add mover_name=mutate/>
    <Add mover=iterate/>
    <Add filter=ddG />
    <Add filter=sasa />
</PROTOCOLS>
</dock_design>
```

[1] talaris2013m corresponds to the talaris2013.wts weighting scheme except for two statistical based energy terms that were modified. The weight of the reference energy term ('ref') was set to 0 and the one penalizing rarely observed rotameric states ('fa_dunbrack') was reduced by 50% and set to 0.28.

[2] talaris2013m_softrep is same as talaris2013m, except that the line 'ETABLE FA_STANDARD_SOFT' was added in the first line of the file to activate the soft repulsion potential.

### *Exploring the Occurrence of Protein-Protein Interfaces which Could Be Targeted by a Tethered Peptide Made of a Helix and a Strand*

To estimate to which extent the epitope tethering approach we used for lengthening Asf1 inhibitory peptides could be generalized to other protein-protein interfaces. In particular we studied the possibility of lengthening an initial helical peptide by a strand providing additional contacts with the target. To this effect, 1,122 biological, non-obligate interfaces of proteins A and B with a known structure were retrieved from the InterEvol database (Faure et al., 2012). We searched dimeric A-B interfaces with a helix on chain A binding to an apolar patch on chain B (the helix can then be extracted as a first epitope binding B) and a nearby apolar patch or β-strand on chain B which can be targeted by a second epitope (possibly a β-strand complementing an existing sheet). Secondary structures were assigned using DSSP (Kabsch and Sander, 1983). Interfaces were searched for helices longer than 4 residues contacting an apolar patch; two levels of stringency were considered, (i) either tight contact, with 3 residues from the helix contacting 3 residues from the patch (contact between two residues is defined as a maximum distance of 8Å between the two Cβ atoms), or (ii) more relaxed constraint, with 2 residues from the helix contacting 2 residues from the patch. Then, two leads were explored:

- search for a second apolar patch nearby, i.e. with at least one residue from the first patch being at a maximum Cβ distance of 16 Å from at least one residue in the second patch;
- search for a "targetable" β-strand nearby (maximum Cβ distance 10Å between at least one residue from the first apolar patch and one residue from the strand AND maximum Cβ distance 12 Å between at least one residue at the helix N- or C-terminus and one residue at the strand N- or C-terminus); the β-strand must belong to a β-sheet defined by DSSP, with exposed backbone O atoms (at least 4 exposed atoms or at least half the strand length);
- this last search was refined by looking for a residue on the side of the strand opposite the helix which would belong to an apolar patch.

We found that around one third of these interfaces (374 interfaces) hold a "helix against apolar patch" motif, with a constraint of tight contact between helix and patch. If this constraint is relaxed and smaller helix-patch contact regions are included, 600 interfaces (half the dataset) contain such a pattern (as described above). Among the 374 interfaces with the "helix against apolar patch" motif, 304 (81%) also contain a nearby apolar patch belonging to the interface which could be targeted by a second tethered epitope. Moreover, 94 out of 374 interfaces (25%) possess a "targetable" β-strand (i.e. an exposed strand from a β-sheet that can be complemented by a designed β-strand) close to the first apolar patch and in most of these (81 interfaces), the targetable β-strand contains a residue belonging to an apolar patch on the side of the strand opposite to the helix (which might be used to anchor the designed complementary strand, using an aromatic residue for instance).

## Proteins and Peptides Production Methods

Peptides were purchased from custom synthesis service (GeneCust) (> 98% purity). For introducing peptides in cells, a N-terminal extension $(RRP)_5$ (Daniels and Schepartz, 2007) with or without a FITC label was added in the synthesis (Table S1). Recombinant human Asf1 (ASF1A(1-204), $ASF1A_N$ (1-156), ASF1B(1-202) and $ASF1B_N$(1-156)) was purified as already described (Mousson et al., 2004) from expression in *E. coli* of a $(His)_6$–GST –Tev site–Asf1 fusion protein using the pETM30 plasmid. Briefly, soluble $(His)_6$-tagged GST fusion proteins were purified on reduced glutathione (GSH) agarose beads (Sigma). After cleavage with recombinant (His)6-TEV protease at room temperature overnight, the (His)6-GST tag and the protease were trapped in a Ni-NTA agarose column (Qiagen). The flow-through fraction containing Asf1 proteins was further purified by anion exchange chromatography using a Resource Q 6mL column (GE Healthcare). Asf1 proteins were concentrated using an Amicon device (Millipore) and the buffer was replaced with a 50mM Tris-HCl (pH7.4). Recombinant Drosophila melanogaster histones H3-H4 (identical to human

histones H3.2) were co-expressed with (His)6-dAsf1 from the pET28 plasmid (generous gift from R.N. Dutnall) from the soluble fraction as already described (Richet et al., 2015) and concentrated using an Amicon device (Millipore) and in a 50mM Tris-HCl (pH7.4), NaCl 2M buffer. Protein and peptide concentrations were determined by UV spectrophotometry (NanoDrop, Thermo Scientific) or Amino-acid Analysis.

## Biochemical and Biophysical Methods

### *Isothermal Titration Calorimetry (ITC)*

All IsoThermal Calorimetry (ITC) experiments were performed in a VP-ITC titration calorimeter (Microcal/Malvern) at 5°C, in a 50mM Tris-HCl pH7.4 buffer. Protein and peptides concentrations were set to values between 5μM-10μM and 50μM-160μM, respectively depending on the measured affinities. Protein and peptide samples were prepared in the same buffer and degassed (ThermoVac, Malvern). After equilibrating the cell at 278°K, the rotating syringe (310rpm) injected at intervals of 280s, 6μL aliquots of peptide solution into the Asf1 previously introduced in the sample cell until saturation was observed. Raw ITC data were processed with the Origin 7.0 Software (OriginLab, Malvern) using the One-Set of Sites fitting model. All ITC experiments were performed at least in duplicate. Two values of the experimental error were considered, i) the mean value of errors calculated from the fit of independent experiments and ii) the standard deviation of fitted values from independent experiments. The experimental error presented in Table 1 was set to the maximal value between both calculations.

### *Circular Dichroïsm Experiments*

Circular Dichroïsm experiments were performed using a Jasco J-815 instrument with a 50μM solution of ip1 and ip1_s at 278°K. The wavelength varied between 190 and 250nm by steps of 1nm. A blank spectra was subtracted and noise smoothing was applied.

### *NMR Experiments*

NMR experiments were carried out on Bruker DRX-600MHz and 700MHz spectrometers equipped with cryoprobes. All NMR data were processed using Topspin (Bruker) and analysed using Sparky (T.D. Goddard and D.G. Kneller, UCSF). Peptide samples were prepared in 5mm NMR tubes, in solution containing D2O 10%, NaN3 0.1%, EDTA 1mM, DSS 0.1mM, pH5.5. TOCSY (80scans with Tmix of 80ms) and NOESY (200scans with tmix of 210ms) were recorded at a temperature of 278.15K. The Hα chemical shift index (CSI) was calculated as follows: CSI=cδ_Hα-rδ_Hα where cδ_Hα is the Hα chemical shift measured of the peptide sample, and rδ_Hα correspond to the reference Hα chemical shift measured in a random coil peptide (Merutka et al., 1995). For some cδ_Hα, an additional correction to the corresponding rδ_Hα was applied as described by (Schwarzinger et al., 2001).

### *Crystallization, Data Collection and Structure Determination*

$ASF1A_N$ -peptide were mixed in a 1:3 ratio and the complex was concentrated to 8mg/mL in a buffer solution of 50mM Tris-HCl pH 7.4 in the presence of the inhibitor protease cocktail at the concentration recommended by the manufacturer (cOmplete, Roche). Crystals of the complex were grown by sitting drop vapour diffusion at 20°C against reservoir solution containing Tris-HCl 0.1M pH7.5, PEG8000 5% for ASF1-ip2_s, Citrate 0.1M pH 2.5, LiSO4 0.25M, PEG8000 7%, for ASF1-ip3, and Citrate 0.1M pH 2.5, LiSO4 0.5M, PEG8000 10%, for ASF1-ip4. Crystals were soaked in a cryo-protectant solution containing reservoir solution supplemented with 30% glycerol, 22.5% xylitol, or 20% glycerol for $ASF1A_N$ _ip2_s, $ASF1A_N$ -ip3, or $ASF1A_N$ -ip4, respectively, and flash-frozen in liquid nitrogen. Diffraction data were collected on the PROXIMA-1, PROXIMA-2 beamlines at the synchrotron SOLEIL (Saint Aubin, France) at a temperature of 100°K with X-ray wavelength of 0.97857Å. Diffraction images were processed using the XDS package (Kabsch, 2010). Structures of ASF1-peptide complexes were solved by molecular replacement using MOLREP (Vagin and Teplyakov, 2010) with the human $ASF1A_N$ structure (PDB ID: 2IO5) as model probe. Model building was performed manually with Coot (Emsley and Cowtan, 2004) and structure refinement was achieved with BUSTER (Bricogne et al., 2017; Smart et al., 2012) or REFMAC (ccp4i suite) (Vagin and Teplyakov, 2010; Vagin et al., 2004). Final refinement statistics are presented in Table S2. Coordinates and Map coefficients were deposited in the Protein Data Base with the following codes: 6F0F, 6F0G and 6F0H for ASF1-ip2_s, ASF1-ip3 and ASF1-ip4 respectively. Structure representations presented in all figures were drawn with PYMOL software (Schrödinger).

### *GST Pull-Down Assays*

1.7 pMol of $(His)_6$-GST-fusion $ASF1A_N$ (ASF1A 1-156) or $(His)_6$-GST-fusion $ASF1B_N$ (ASF1B 1-156) immobilized on 20μL of reduced glutathione agarose beads were equilibrated with 200μL of buffer H1000 (50mM Tris-HCl pH 8, 1M NaCl, 0.5% NP40, 1 mM EDTA, 1mM DTT). An excess of purified histones H3-H4 (3.5 pMol) solubilized in the same buffer was added in a final volume of 400μL and incubated overnight at 4°C under gentle agitation. Beads were washed five times with 400μL of buffer H150 (same as H1000 except with 150mM NaCl) to remove unbound histones. 50μL were collected for SDS-PAGE analysis (Beads before elution BBE). Beads were then incubated overnight in 100 μL of peptides at different concentrations (0, 5, 10, 50 and 100μM) in the buffer H150. Then, bound and eluted proteins were analyzed by SDS-PAGE followed silver staining. 5μL for BBE and 15μL for peptide elution were respectively loaded on the gel as shown in Figure 3A.

### *Proteomics and Liquid Chromatography Coupled to Mass Spectrometry (LC-MS/MS) Analysis*

Pulldown with biotinylated peptides were performed as described below. Strep-tactin superflow resin after 5 washes with PD buffer and proteins on sepharose beads were washed twice with 100μL of 25mM NH4HCO3 and we performed on-beads digestion with 0.2μg of trypsine/LysC (Promega) for 1 hour in 100μL of 25mM NH4HCO3. Sample were then loaded onto a homemade C18 StageTips for desalting. Peptides were eluted using 40/60 MeCN/H2O + 0.1% formic acid and vacuum concentrated to dryness.

Peptide samples were resuspended in buffer A (2/98 MeCN/H2O in 0.1% formic acid), separated and analyzed by nanoLC-MS/MS using an RSLCnano system (Ultimate 3000, Thermo Scientific) coupled online to an Orbitrap Fusion Tribrid mass spectrometer (Thermo Scientific). Peptides were trapped on a C18 column (75 μm inner diameter × 2 cm; nanoViper Acclaim PepMapTM 100,

Thermo Scientific) with buffer A at a flow rate of 4.0 μL/min over 4 min. Separation was performed on a 50 cm x 75 μm C18 column (nanoViper Acclaim PepMapTM RSLC, 2 μm, 100Å, Thermo Scientific) regulated to a temperature of 55°C with a linear gradient of 5% to 25% buffer B (100% MeCN in 0.1% formic acid) at a flow rate of 300 nL/min over 100 min. Full-scan MS was acquired in the Orbitrap analyzer with a resolution set to 120 000 and ions from each full scan were HCD fragmented and analyzed in the linear ion trap.

For identification, the data were searched against the Homo sapiens Swiss-Pro database using SEQUEST proteome discoverer (version 2.2), one by one or merged per conditions for emPAI abundance evaluation (Yang et al., 2013). Enzyme specificity was set to trypsin and a maximum of two-missed cleavage sites were allowed. Oxidized methionine and N-terminal acetylation were set as variable modifications. Maximum allowed mass deviation was set to 10 ppm for monoisotopic precursor ions and 0.6 Da for MS/MS peaks.

The resulting files were further processed using myProMS (v3.6) (Poullet et al., 2007). FDR calculation used Percolator and was set to 1% at the peptide level for the whole study. The label free quantification was performed by peptide Extracted Ion Chromatograms (XICs) computed with MassChroQ version 2.2 (Valot et al., 2011). For protein quantification, XICs from proteotypic peptides shared between compared conditions (TopN matching) were used. Median and scale normalization was applied on the total signal to correct the XICs for each biological replicate. To estimate the significance of the change in protein abundance, a linear model (adjusted on peptides and the three independent biological replicates) was performed and p-values were adjusted with a Benjamini–Hochberg FDR procedure with a control threshold set to 0.05. All hits were ranked using exponentially modified proteins abundance index (emPAI) weight % (Yang et al., 2013) in Table S3. The mass spectrometry proteomics data have been deposited to the ProteomeXchange Consortium via the PRIDE (Deutsch et al., 2017) partner repository with the dataset identifier PXD013279.

## Cell Biology Methods

### *Immuno-precipitation of endogenous ASF1A and ASF1B*

*i) Preparation of Cytosolic and Salt-Extractable Extracts*. Dry cell pellets of HeLa S3 cells were suspended in 3 volumes of cold hypotonic buffer [20mM HEPES-KOH pH 7.0, 0.15mM Ethylenediaminetetraacetic acid (EDTA-KOH) pH 8.0, 0.15mM triethylene-glycol-diamine-tetraacetic acid (EGTA-KOH) pH 8.0, 10mM KCl, 0.15mM spermine , 0.15mM spermidine, 1mM DTT, protease and phosphatase inhibitors cocktails (Roche, Cat#11873580001 and Cat#4906845001 respectively)], supplemented with NP-40 at final concentration 1% (v/v), and mix gently. After addition of 8/9 V of SR buffer [50mM HEPES-KOH pH 7.0, 0.25mM EDTA-KOH pH 8.0, 10mM KCl, 70% (m/v) sucrose, 1mM DTT, 0.15mM spermine, 0.15mM spermidine, phosphatase and protease inhibitors] cytosolic fraction and nuclei were separated by centrifugation for 5 min at 2000 x g at 4°C. Nuclei pellet was resuspended (v/v) in low salt buffer [20mM Hepes KOH pH 7.8, 0.5mM MgCl2, 5mM C2H3O2K pH 5.5, 10% glycerol, 1mM DTT, phosphatase and protease inhibitors], supplemented drop wise with high salt buffer [20mM HEPES-KOH pH 7.8, 0.5mM MgCl2, 5mM C2H3O2K pH 5.5, 10% glycerol, 1.6 MNaCl, 1mM DTT, phosphatase and protease inhibitors] to reach final 540mM NaCl, incubated for 90 min on ice with mixing, diluted with equal volume of low salt buffer, centrifuged at 20 000 x g for 20 min. Supernatant (salt extractable extracts) was mixed with cytosolic extracts and centrifuged at 100 000 x g for 30 min;

*ii) Immunoprecipitation*. For each condition 1mg of total extract was then supplemented with 25nmol of corresponding inhibitor peptide and incubated for 1h at 4°C in IP Buffer [20mM Tris-HCl pH 7.5, 15mM KCl, 150mM NaCl, 10% glycerol, 0.1mM EDTA-NaOH, pH 8.0, 0.01% NP40, 1mM DTT, phosphatase and protease inhibitors] prior overnight incubation with 1μg of purified specific ASF1 antibodies or rabbit IgG. Complexes were isolated by incubation with protein A/G resin (ThermoFisher Cat#53132) for 2h at 4°C. After five washes in IP Buffer, beads were suspended in NuPage LDS Sample Buffer (ThermoFisher NP0007) supplemented with NuPAGESample Reducing Agent (ThermoFisher NP0009), boiled for 10 min, and the supernatant was then loaded onto a NuPage 4–12% Bis-Tris gel (ThermoFisher), transferred on PVDF or 0.2μm nitrocellulose membrane using TransBlot Turbo system (BioRad) for further Western Blot analysis. We used secondary antibodies conjugated with Horseradish peroxidase (Interchim) and revealed the signal by chemiluminescence with SuperSignal West Dura Extended Duration Substrate (ThermoFisher Cat#34076). The signal was acquired using ChemiDoc Imager (Biorad).

### *Pulldown with Biotinylated peptides*

*i) Preparation of the Total Extracts*. Dry cell pellets of HeLa S3 cells were resuspended in equal volume of the cold lysis buffer [50mM Tri-HCl, pH 7.5, 300mM NaCl, 0,5% NP-40, 10% glycerol, 2mM MgCl2, 10μM CaCl2, 5mM EGTA-KOH pH 8,0, 1mM DTT, phosphatase and protease inhibitors] and incubated for 30 min at 4°C. The lysate were then supplemented with CaCl2 up to 1mM and treated with 0,0025U/μl MNase (Sigma N3755) for 12 min at 37°C. The reaction was stopped by addition of EDTA-NaOH, pH 8.0 up to 4mM. Extracts were centrifuged at 100 000 x g for 30 min. Supernatant was diluted with equal volume of dilution buffer [50mM Tris-HCl, pH 7.5, 1 % glycerol, 100mM KCl, 5mM EGTA-KOH pH 8.0, 1mM DTT, phosphatase and protease inhibitors].

*ii) Pulldown*. For each condition 1mg of total extract was then precleared with Superflow6 resin (IBA) for 30 min at 4°C, supplemented with 25 nmol of corresponding inhibiting peptide and incubated overnight at 4°C in PD Buffer [20mM Tris-HCl, pH 7.5, 150mM NaCl, 0.2mM EDTA-NaOH pH 8.0, 0.1% NP-40, 5% Glycerol, 1mM DTT, protease inhibitors]. The extracts were then incubated with Strep-tactin Superflow resin (IBA) for 2h at 4°C in PD Buffer. After five washes in PD buffer [150 mM NaCl] or with two washes with PD buffer followed by two washes with PD Buffer containing 500mM NaCl and then one wash with PD buffer [500 mM NaCl wash], the beads were equilibrated in elution buffer (PD buffer supplemented with 10mM D-biotin) and incubated for 10 min at RT. The resulting eluent was resuspended in NuPAGE LDS Sample Buffer, boiled, and analyzed by SDS-PAGE and Western Blot (Figure 3C). For each antibody, all presented samples were run on a same gel. For a sake of clarity, lane order was modified. Cuttings are made explicit with white spaces.

### U2OS Cell Transfection with siRNA ASF1A and ASF1B

We transfected U2OS cells were reverse transfected with siRNAs against ASF1A [ID: s226043, ThermoFisher] and ASF1B [ID: s31345, ThermoFisher] using Lipofectamine RNAiMAX (Life Technologies) according to manufacturer's instruction. Briefly, siRNAs were complexed with Lipofectamine for 15 minutes in 96 well black-walled, clear bottom plates (Costar #3904). U2OS cells were then seeded on top of the lipoplexes (6 000 cells/well; final [siRNA]=5nM or 10nM; combination [siRNA ASF1A] 5nM + [siRNA ASF1B] 5nM) and plates were incubated for 48h at 37°C and 5% $CO_2$. A commercial mixture of cytotoxic siRNAs (AllStars Maximal Death Control, Qiagen) and a scrambled siRNA (Cat#4390843, Silencer Select #1 sequence, ThermoFisher) were used as positive and negative controls, respectively.

### Nucleofection of Green Fluorescent Fusion-Inhibitory Peptide Genes in a Mammalian Expression Vector

Oligonucleotides encoding the Asf1 inhibitory peptides ip3, ip4 or the negative control ip3mut3A peptide were introduced in a mammalian expression vector via the Gateway technology (Invitrogen) with the pDONR207 to obtain pENTR, and pENTR with pDEST53 following manufacturer's instructions (Invitrogen) to obtain vectors expressing GFP-tagged peptides. The plasmids were delivered in in U2OS cells by nucleofection using the Amaxa Cell Line Nucleofector Kit V (Lonza) according to the manufacturer's instructions. Cells were then seeded in standard 6 well plates or black-walled, clear bottom, 96-well culture plates (Costar, Cat#3904) at 15 000 cells/well and incubated 24h at 37°C with 5% $CO_2$. Green Fluorescent protein (GFP) fused peptides were observed with a DMIRE2 apparatus (Leica) at 40X magnification. GFP fluorescence was quantified using flow cytometry to adjust plasmid amounts to obtain equivalent peptide expression for all constructs.

### Co-Immunoprecipitation of GFP-Tagged Inhibitory Peptides with ASF1A and ASF1B

48 hours after nucleofection, $2x10^6$ U2OS cells were harvested and washed with ice-cold PB buffer (100mM Potassium Acetate, 3mM KCl, 10mM $Na_2HPO_4$, 1mM $MgCl_2$ and protease inhibitors cocktail as recommended by the manufacturer [cOmplete, EDTA-free; Roche]) and centrifuged 5 minutes at 290 × g. All further steps were performed at 4°C. Cell pellets were resuspended and incubated 20 minutes in 400μL of lysis buffer (PB buffer + 200mM NaCl, 0.2% v/v Triton X-100). Lysates were cleared by centrifugation for 1 hour at 16 000 × g. Supernatants were incubated with 30μL of magnetic anti-GFP beads (μMACS Anti-GFP MicroBeads; Miltenyi Biotec) for 30 minutes under gentle agitation. Beads were then transferred into μColumns (Miltenyi Biotec) installed on top of a magnetic rack (Miltenyi Biotec), and washed with 500μL lysis buffer. Beads were eluted from the column with 25μL of lysis buffer. Proteins in the supernatant (Input) and bound to the beads (IP) were analysed by SDS PAGE and detected by western blotting using a polyclonal antibody against anti-ASF1B (ASF1B [C70E2, 1/400] Rabbit mAb; Cell Signaling); rabbit anti-ASF1A (ASF1A [C6E10, 1/10000] Rabbit mAb; Cell Signaling); rabbit anti-GFP (Anti-GFP antibody [ab290, 1/10000]; Abcam and mouse anti-GAPDH). GAPDH and GFP were used as controls of sample loading and peptide expression, respectively. Results are presented Figure 4B. For each antibody, all Input samples or IP samples were run on a same gel. For a sake of clarity, lane order was modified. Cuttings are made explicit with white spaces.

### Cell Proliferation/Survival Using MTT Assay

Impact of expression of Asf1 inhibitory peptides on proliferation/survival of U2OS cell lines was assessed using the methyl thiazolyl tetrazolium (MTT) assay (Mosmann, 1983). Sterile MTT (M5655, Sigma Aldrich) was dissolved in PBS buffer and added to the cells at a final concentration of 1mg/ml and cells were incubated at 37°C with 5% $CO_2$ for 3 hours. Culture medium was discarded and cells incubated overnight at 37°C with the lysis buffer 20% SDS, 33% N,N-dimethylformamide, 2% acetic acid, 25mEq/L HCl, pH4.5 adjusted with NaOH 10N. Light absorbance was measured with the Multiskan™ FC Microplate Photometer (Thermo Scientific) at 570nm and 620nm after transfer of 200μL of lysate into a 96-well plate (655185, Greiner CellStar®). The effect of inhibitory peptides was calculated as a percentage of the treated and untreated cells signal (A570 – A620 of treated cells)/(A570 – A620 of control cells) × 100, where A refers to the absorbance at the indicated wave length. Results are presented Figure S5D.

### Transduction of CPP-Vectorized Peptides in U2OS Cells

U2OS were seeded at 6 000 cells/well in 96-well format for 24 hours at 37°C, 5% CO2 then CPP-peptides (See Table S1 for the corresponding sequences) were added directly into the culture medium (v/v) at gradient final concentration of 1μM, 5μM and 10μM. Cells were then incubated 24h at 37°C and 5% $CO_2$.

### Cell Proliferation/Survival and Cell Cycle Profiling of U2OS Cells with High Content Imaging (HCI)

To quantify cell proliferation/survival and cell cycle, cells were fixed with PFA 2% final (v/v) nucleic acids were stained with Hoechst 33342 [Sigma] at 2 μg/mL final. After overnight incubation at 4°C in the dark, cell supernatants were then replaced with PBS, and plates were submitted to image acquisition with an automated epifluorescence High-Content Imaging System (Operetta, Perkin Elmer). Nine fields per well were acquired at 10X magnification, in two fluorescence channels: red for Propidium Iodide (ex: 535±15nm em: 595±35nm) and blue for Hoechst 33342 (ex: 380±20nm; em: 445±35nm). An automated algorithm was developed under Harmony 3.0 (Perkin Elmer) to quantify the relative cell proliferation/survival and to quantify genomic DNA amount based on Hoechst fluorescence. Briefly, nuclear Regions of Interest (ROI) were segmented in the Hoechst channel, and cell proliferation/survival was expressed as the nuclear ROI amount in sample conditions relative to those in controls. For cell cycle measurement, the integrated, background-corrected Hoechst fluorescence intensities were quantified for more than 6000 cells. Cell cycle profiles were established by classifying nuclei frequency in 100 fluorescence intervals encompassing the G1 to G2/M phases (arbitrary units). A smoothing of the distribution curves with a window of 5 intervals and a normalization for the total number of cells was applied.

### U2OS Cell Cycle Measurement by Flow Cytometry

Cell cycle presented in Figure 4E was performed by flow cytometry using a double labelling with Propidium Iodide (PI) and 5-Bromo-2-deoxyuridine (BrdU). U2OS cells were incubated 15min at 37°C and 5% $CO_2$ after addition of BrdU at a final concentration of 50μM

in the culture medium. All cells were collected in PBS and fixed with -20°C cold ethanol 70% (v/v) overnight at 4°C. BrdU incorporation was quantified by immunofluorescence after treatment of cells with Pepsine/HCl solution (0.5mg/mL pepsine, 30mM HCl) for 20 min at 37°C, followed by lysis with 2M HCl for 20min at room temperature. Acidity was neutralized with a buffer containing 20mM Hepes, 0.5% (v/v) Tween20 in DPBS. After centrifugation (5min, 1200 x g), the supernatant was discarded, pellets were resuspended and incubated for 1h at RT with mouse anti-BrdU primary antibody (Cat#347580BD Biosciences) dissolved 1/100 in the buffer (50mg/mL BSA, 0.1% [v/v] Tween20 in DPBS). The pellet was incubated 1 hour at RT with anti-mouse Alexa 488 (Cat#A11029, Life Technology) 1/100 in same buffer. Genomic DNA was labelled for 20 minutes on ice with 40μg/mL PI (P4864, Sigma Aldrich) in PBS containing 40μg/mL RNase (R6513, Sigma Aldrich). Flow cytometry analysis was performed using a FACS-Calibur instrument (BD Biosciences) with the excitation 488nm laser and the observation in the FL1 channel (Emission: 530±30nm) and in the FL2 channel for PI (Emission: 585±42nm) at a rate of 300cells/s. A total of 10 000-20 000 events were recorded for each sample. Compensation of 10% was applied after acquisition in the FL2 (PI) channel with respect to the FL1 (A488) channel. For cell cycle analysis presented in Figure S6C, a double labelling with Click-iT 5-ethynyl-2'-deoxyuridine (Click-iT EdU), Ca#C10632, Thermofisher) according to the manufacturer's instructions and with Hoechst for DNA content labelling was performed. Briefly, cells were incubated 15 min at 37°C and 5% CO2 after addition of Click-iT EdU, then permeabilized and fixed with the Saponin-BSA buffer provided in the kit. The fluorescent Alexa-Fluor 647 Azide (A10277, Thermofisher) was added in the Click-iT reaction cocktail. Hoechst was added at a final concentration of 2 μg/mL and cells were incubated overnight in the dark at 4°C. Flow cytometry analysis was performed a MoFlo Astrios instrument (Beckman-Coulter, Roissy CDG, France) after addition of 40μg/mL RNase (R6513, Sigma Aldrich) and Triton 0.15% (v/v). Hoechst fluorescence was excited by a 355-nm laser (100 mW), taking emission at 432–482 nm. Edu-AlexaFluor647 was excited by a 640-nm laser (60 mW). A total of 15 000 events were recorded for each sample.

#### *Cell Viability on Mouse 4T1 Cells Using PrestoBlue® Viability Assay*

Cell viability of mouse 4T1 cells upon Asf1 inhibitory peptides treatment was measured using PrestoBlue® assay (Thermofisher). 4T1 cells were seeded in a 96-well plate at a concentration of $3.3\times10^4$ cells per well. Cells were allowed to attach for 24 hours at 37°C then, vehicle ($H_2O$) or different concentrations of ip3mut3A, ip3 or ip4 peptides (10μM to 30μM) were added in the culture medium once a day during 48 h. Thereafter, 10μL of PrestoBlue was added to each well and cells were incubated for an additional hour at 37°C. Fluorescence was subsequently read at 580nm, using a FluoStar Optima plate reader (BMG LabTech, Ortenberg/Germany).

#### *Migration and Invasion Assay of 4T1 Cells*

4T1 cells in culture were trypsinized, counted and resuspended in serum-depleted medium (0.5% FBS), and plated at $1.10^4$ cells per transwell in 24-well Boyden chamber plates for migration assay (BD Biosciences) or in 24-well Matrigel Invasion chamber plates (BD BioSciences) using 10 % FBS as chemoattractant. After 6 h of treatment with 10μM ip3mut3A, ip3 or ip4 for migration assay or 24 hours for invasion assay, migratory or invasive cells were fixed with paraformaldehyde and stained with 0.04% crystal violet. The number of cells that migrated through the membrane was counted visually within each entire well using the Axio Observer Microscope Z1 (Zeiss) and image stitching (Axiovision 4.8.2 software, Zeiss).

### In Vivo Experiments Methods

#### *Tumour Growth Experiments*

Balb/c mice (10 weeks old, 20-25g) were obtained from Janvier Labs (France). Five female mice were used for each group. 4T1 cells ($5\times10^5$ cells in a mixture of 50μl of medium and 50μL of Matrigel) were injected subcutaneously into the hind flank of the animals. When the tumours reached 50-100 $mm^3$ in size (5 to 8 days post-implantation), mice were randomized into three groups and vehicle, ip3mut3A, ip3 or ip4 peptides were injected every other day into the tumours (100μg/injection). Tumour size was monitored by caliper measurement of tumour length and width every other day. Tumour volume was calculated according to the formula $V = 0.5 \times (A \times B^2)$ where A and B were the largest and the smallest diameters, respectively. Studies were ended when tumours in the control group reached an average of 1000 $mm^3$ (day 14). Mice were sacrificed by cervical dislocation and tumours were excised and fixed in 4 % (w/v) paraformaldehyde to perform immunohistochemistry.

#### *Immunohistochemistry*

5 μm sections of paraffin-embedded tumours from each group were deparaffinised in xylene and rehydrated. For VEGF, GLUT1, PCNA and active Caspase-3 immunodetection, 5-μm-thick paraffin sections of PFA-fixed tumours were deparaffinised, rehydrated and microwaved (900 W for 2 x 5 min) in 10 mM citrate buffer pH 6. Endogenous peroxidase activity was blocked by incubating sections with 1% $H_2O_2$ in methanol for 20 min. Slides were subsequently incubated in TBS buffer containing 5% goat serum (X0907, DAKO) and 2% BSA for 20 min, then overnight at 4°C with anti-human VEGF-A (1/200, Sc-152, Santa Cruz), anti-GLUT1 (1/200, ab15309, Abcam), anti-PCNA (1/6000, ab29, Abcam) or anti-cleaved Caspase 3 antibodies (1/200, Cat#9664, Cell Signaling). After two washes of 5 min in TBS containing 0.1% Tween 20, sections were sequentially incubated for 1 h with biotinylated anti-rabbit secondary antibodies for VEGF, GLUT1 and cleaved Caspase 3 (Vectastain ABC kit, PK6101, Vector) or biotinylated anti-mouse secondary antibodies for PCNA staining (Vectastain ABC kit, PK6102, Vector) and for 45 min with avidin/biotinylated horseradish peroxidase complex (Vectastain ABC kit, Vector). Peroxidase activity was revealed using diaminobenzidine tetrachloride as a chromogen (K3468, DAKO). Control sections were incubated with a pool of secondary antibodies in the absence of primary antibodies. Sections were briefly counterstained with hematoxylin (Sigma-Aldrich), dehydrated and mounted. Slides were observed using a Zeiss Axioplan microscope equipped with an Axiocam HRC camera and Axiovision software version 4.8.

## QUANTIFICATION AND STATISTICAL ANALYSIS

Statistical analysis was performed with the software Prism 7.03 (GraphPad). Values are expressed as means ± SEM of the number of independent experiments and number of replicates indicated in each figure legends. Significance was determined by a t-test with (****) $P < 0.0001$; (***) $P \leq 0.0005$; (**) $P \leq 0.005$; (*) $P \leq 0.05$; (NS) not significant.

## DATA AND CODE AVAILABILITY

The accession numbers for the ASF1-ip2_s, ASF1-ip3 and ASF1-ip4 structures reported in this paper are PDB: 6F0F, PDB: 6F0G and PDB: 6F0H respectively.

The accession number for the Mass spectrometry proteomics data for pulldowns with biotinylated peptides ip3mut3A and ip4 reported in this paper is ProteomeXchange: PXD013279).